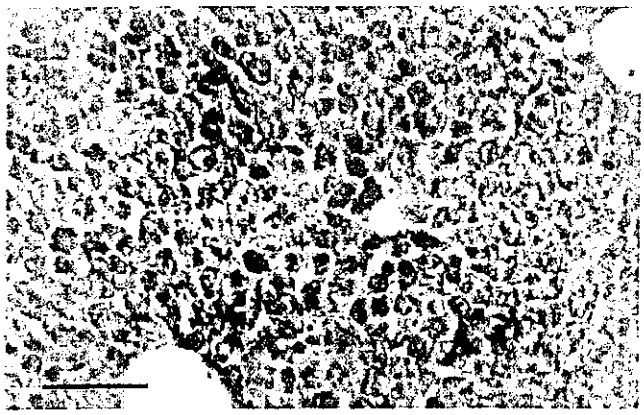

*Figure 5 X-gal staining of the liver in a treated mouse at the 30th day. Many positive-staining cells were spread diffusely in the whole organ. Scale bar=100 μm.*

blood–brain barrier would be definitely different between at 24 h and at 48 h because the brain of the newborn mouse develops very rapidly.

The activities of β-galactosidase were very much increased in the liver, lung, and the heart (Table 1), where the high vascularity and abundant blood flow may give predominance of adenovirus infection. Moreover, large deviations of activity among the treated mice would suggest that the activity resulted from the infectious efficiency. The primary source of β-galactosidase activity is speculated to be direct infection by adenovirus, not cross-correction by secreted enzyme. This hypothesis is supported by the fact that the activities in each organ in treated mice were not parallel among the organs (Figure 1). In other words, the mouse having the highest activity in the liver did not necessarily have the highest activity in the brain, and *vice versa*.

Although the direct infection of tissues by adenovirus vector seems to be the primary source of β-galactosidase activity, interorgan and intraorgan cross-correction by circulating enzyme must also be a factor. The interorgan cross-correction might play a major role in the early stage of infection when high levels of serum activity are present. Since the blood–brain barrier is not fully intact until 10–14 days of life in rodents,[21] it would be possible for the proteins to enter from blood flow into the brain, as well as for the virus particles. The evidence of intraorgan cross-corrections was shown both in the brain and in the liver of this study. The remarkable attenuation of ganglioside GM1 accumulation in the brain and the liver was shown in some treated mice by biochemical analysis, while only a small number of cells (less than 1 and 10% of the cells in the brain and in the liver, respectively) were positive with X-gal staining (Figures 3 and 5). Since the infected cells are the only source of the β-galactosidase activity in the brain after the closure of the blood–brain barrier, the vector expressing the enzyme activity constitutively is needed for the successful prevention of the disease. As the maturation of blood–brain barrier in the human, which is completed by birth, is definitely different from that in the mouse, intrauterine treatment may be needed for human patients. However, the treatment before the massive accumulation occurs is important definitely, and it would be possible that the low level but persisting activity of the enzyme could prevent the further accumulation and the disease development throughout life.

## Materials and methods

### GM1-gangliosidosis mouse model (β-galactosidase-deficient mouse)

Mouse model of GM1 gangliosidosis was generated by targeting of β-galactosidase gene in ES cells as previously described.[22,23] Newborn mice were obtained by mating the heterozygous female mice with the homozygous male mice. Identification of newborn mutants was accomplished by quantitative analysis of β-galactosidase activity in the tail tip homogenates on the day of birth. Age-matched wild-type mice of C57BL/6 strain were used as the control.

All surgical and care procedures were carried out according to the Guidelines for Use and Care of Experimental Animals approved by the Animal Committee of Osaka City University School of Medicine.

### Construction of adenovirus vector with β-galactosidase cDNA

AdEasy system,[24] the system for constructing adenovirus vector, was kindly provided by Dr. Vogestein at Johns Hopkins Oncology Center. Mouse β-galactosidase cDNA was cloned and constructed as previously reported.[25] Construction of adenovirus vector carrying mouse β-galactosidase cDNA was performed by the protocol described at http://www.coloncancer.org/adeasy/protocol.htm. Mouse β-galactosidase cDNA was cloned into the shuttle vector pAdTrackCMV having GFP gene as a reporter, linearized by digesting with *PmeI*, and cotransformed by electroporation with an adenoviral backbone plasmid pAdEasy-1 into *E. coli* BJ5183 cells. Recombinants were selected for kanamycin resistance, and linearized by digesting with *PacI*, then transfected by Lipofectamine (GIBCO BRL, Rockville, MD, USA) into the 293 adenovirus packaging cells. Recombinant adenoviruses were generated within 7–12 days. The recombinant virus solution was obtained by removing the host cells by sonication and centrifugation. The virus was amplified by repeating the infection with the viral supernatant. The concentration of viral solution was achieved finally at $3.93 \times 10^9$ PFU/ml.

To confirm the virus activity, infection to HeLa cells was performed at an MOI of 40. The infection and the protein formation by the recombinant virus were determined by GFP fluorescence on microscope and the analysis of β-galactosidase activity in the cell homogenate and in the culture medium.

### Administration of adenovirus vector and the preparation of tissues

Each mouse received a single intravenous injection of 100 μl of viral suspension with $4 \times 10^7$ PFU via the superficial temporal vein from 24 to 48 h after birth. Mice were examined on the 30th and the 60th days after birth. One hemisphere of the brain was used for biochemical analyses, and the other was used for histological examinations in each mouse.

For the biochemical analysis, mice were anesthetized with diethylether and the blood was washed out with

normal saline by perfusing through the heart, and each organ was wrapped with Parafilm and kept at −80°C until use. For the histological studies, the organs were fixed by perfusing through the heart with 4% paraformaldehyde in 0.1 M phosphate buffer pH 7.4 (PB) for 20 min, after washing out the blood with normal saline. The organs were placed in the same fixing mixture overnight for paraffin sections. For the use of frozen sections, the tissues were placed in 0.1 M phosphate buffer pH 7.4 containing 30% sucrose, then frozen in liquid nitrogen.

### *β-Galactosidase assay*

β-Galactosidase activity was analyzed in the tissue homogenate with the artificial substrate of 2 mM 4-methylumbelliferyl β-galactoside at pH 4.0 in 0.1 M sodium citrate-phosphate buffer according to the method described by Suzuki.[26] The protein was analyzed by using Bio-Rad protein assay system (Bio-Rad Laboratories, Hercules, CA, USA) of Bradford.[27]

### *Ganglioside analysis*

Lipid extraction, ganglioside isolation, and lipid quantification were performed as described by Fujita *et al*[28] and Hahn *et al*[29]. Total lipids were extracted from tissue homogenate in chloroform–methanol (1:2, v/v). Neutral and acidic fractions were separated by reverse-phase column of Varian Bond Elute C-18 (GL Sciences Inc, Tokyo, Japan). The column was preconditioned with chloroform–methanol (1:2, v/v) and 99.5% methanol. The lipids extracted from 100 to 200 mg in wet weight of each tissue were applied onto the column, and the column was washed with methanol–0.9% saline (1:1, v/v). Ganglioside/acidic lipids were eluted with methanol–water (12:1, v/v) and collected for the study. The content of sialic acid in the ganglioside/acidic lipid fraction was analyzed by the colorimetric assay by the resorcinol method[30] with *N*-acetylneuraminic acid as the standard. Lipids were separated by TLC with high-performance thin-layer plates (Merck High-Performance TLC 60; Merck KGaA, Darmstadt, Germany) and developed in the solvent of chloroform–methanol–0.2% $CaCl_2$ (55:45:10; v/v/v). Gangliosides were visualized by resorcinol spray and heating. Each sample was applied in two lanes and repeated twice to show the reliability of the TLC technique. Densitometric quantification of gangliosides was performed using Kodak Digital Science™ EDAS 120 system with 1D Image Analysis software (Eastman Kodak Company, NY, USA). The analysis was carried out within the linear range with respect to the quantity of the lipid using commercially purchased ganglioside GM1 (Sigma G7641, Sigma, MO, USA) as the standard.

### *Histopathological study*

Paraffin sections (10 μm thick) were processed and used for hematoxylin/eosin staining. Frozen sections (15 μm thick) were reacted with X-gal by β-Gal staining Kit (Invitrogen Corp., Carlsbad, CA, USA) to visualize β-galactosidase activity. Ganglioside GM1 accumulated in the brain was visualized in frozen sections by immunostaining of avidin:biotinylated enzyme complex method with anti-GM1 ganglioside monoclonal antibody conjugated with biotin (Seikagaku Corp., Tokyo, Japan) and VECTASTAIN™ ABC Kit (Vector Laboratories, CA, USA). The staining procedures were carried out according to the instructions of the company.

The percentage of the infected cells was analyzed in the brain and the liver specimen stained with X-gal by measuring the blue-stained areas in the pictures.

## *Acknowledgements*

We thank Dr Junichiro Matsuda at the National Institute of Infectious disease, Tokyo, for providing us β-galactosidase knockout mouse. We also thank Dr Kunihiko Suzuki in the University of North Carolina at Chapel Hill, and Dr Marie T Vanier in University of Lyon, France, for their critical readings of the manuscript and many helpful suggestions.

This work was supported by grants AT-11694306 and AT-11557060 from the Ministry of Education, Culture, Sports, Science, and Technology of Japan.

## *References*

1 Birkenmeier EH *et al*. Increased life span and correction of metabolic defects in murine MPSVII after syngeneic bone marrow transplantation. *Blood* 1991; 78: 3081–3092.
2 Ohashi T *et al*. Adenovirus-mediated gene transfer and expression of human β-glucuronidase gene in the liver, spleen, and central nervous system in mucopolysaccharidosis type VII mice. *Proc Natl Acad Sci USA* 1997; 94: 1287–1292.
3 Konfeld S. Trafficking of lysosomal enzyme. *FASEB J* 1987; 1: 462–468.
4 Sands MS *et al*. Murine mucopolysaccharidosis type VII: long term therapeutic effects of enzyme replacement and enzyme replacement followed by bone marrow transplantation. *J Clin Invest* 1997; 99: 1596–1605.
5 Kakkis ED, Muenzer J, Tiller GE, Waber L. Enzyme replacement therapy in mucopolysacharidosis I. *N Engl J Med* 2001; 344: 182–188.
6 Hoogerbrugge PM *et al*. Allogenic bone marrow transplantation for lysosomal storage diseases. *Lancet* 1995; 345: 1398–1402.
7 Suzuki K *et al*. The Twitcher mouse: central nervous system pathology after bone marrow transplantation. *Lab Invest* 1998; 58: 302–309.
8 Matzner U *et al*. Long-term expression and transfer of arylsulfatase A into brain of arylsulfatase A-deficient mice transplanted with bone marrow expressing the arylsulfatase A cDNA from a retroviral vector. *Gene Therapy* 2000; 7: 1250–1257.
9 Pastores GM, Sibille AR, Grabowski GA. Enzyme therapy in Gaucher disease type I: dosage efficacy and adverse and effects in 33 patients treated for 6 to 24 months. *Blood* 1993; 82: 408–416.
10 Desnick RJ, Banikazemi M, Wasserstein M. Enzyme replacement therapy for Fabry disease, an inherited nephropathy. *Clin Nephrol* 2002; 57: 1–8.
11 Imaizumi M *et al*. Long term effects of bone marrow transplantation for inborn errors of metabolism: a study of four patients with lysosomal storage disease. *Acta Pediat Jpn* 1994; 36: 30–36.
12 Elliger SS *et al*. Elimination of lysosomal storage in brains of MPS VII mice treated by intrathecal administration of an adeno-associated virus vector. *Gene Therapy* 1999; 6: 1175–1178.
13 Frisella WA *et al*. Intracranial injection of recombinant adeno-associated virus improves cognitive function in a murine model of mucopolysaccharidosis type VII. *Mol Ther* 2001; 3: 351–358.
14 Shen JS, Watabe K, Ohashi T, Eto Y. Intraventricular administration of recombinant adenovirus to neonatal Twitcher mouse leads to clinicopatholgical improvements. *Gene Therapy* 2001; 8: 1081–1087.

15 Sands MS *et al*. Syngenic bone marrow transplantation reduces hearing loss associated with murine mucopolysaccharidosis type VII. *Blood* 1995; **86**: 2033–2040.
16 O'Connor LH *et al*. Enzyme replacement therapy for murine mucopolysaccharidosis type VII leads to improvements in behavior and auditory function. *J Clin Invest* 1998; **101**: 1394–1400.
17 Volger C *et al*. Enzyme replacement therapy in murine mucopolysaccharidosis type VII: neuronal and glial response to β-glucuronidase requires early inhibition of enzyme replacement therapy. *Ped Res* 1999; **45**: 838–844.
18 Day TM *et al*. Neonatal gene transfer leads to widespread correction of pathology in a murine model of lysosomal storage disease. *Proc Natl Acad Sci USA* 1999; **96**: 11288–11294.
19 Day TM *et al*. Prevention of systemic clinical disease in MPS VII mice following AAV-mediated neonatal gene transfer. *Gene Therapy* 2001; **8**: 1291–1298.
20 Suzuki Y, Oshima A, Nanba E. β-Galactosidase deficiency (β-galactosidosis): GM1 gangliosidosis and Morquio B disease. In: Scriver CR, Beaudet AL, Sly WS, Valle D (eds) *The Metabolic and Molecular Bases of Inherited Disease*, 8th edn. McGraw-Hill: New York, 2001, pp 3775–3803.
21 Stewart PA, Hayakawa EM. Interendothelial junctional change underlie the developmental 'tightening' of the blood–brain barrier. *Dev Brain Res* 1987; **32**: 271–281.
22 Matsuda J *et al*. Neurological manifestations of knockout mice with β-galactosidase deficiency. *Brain Dev* 1997; **19**: 19–20.
23 Matsuda J *et al*. β-Galactosidase-deficient mouse as an animal model for GM1-gangliosidosis. *Glycoconjugate J* 1997; **14**: 729–736.
24 He TC *et al*. A simplified system for generating recombinant adenoviruses. *Proc Natl Acad Sci USA* 1998; **95**: 2509–2514.
25 Nanba E, Suzuki K. Molecular cloning of mouse acid β-galactosidase cDNA : sequence, expression of catalytic activity and comparison with human enzyme. *Biochem Biophys Res Comm* 1990; **173**: 141–148.
26 Suzuki K. Enzymatic diagnosis of sphingolipidosis. *Methods Enzymol* 1987; **138**: 727–762.
27 Bradford MM. A rapid and sensitive method for the quantitation of microgram quantities of protein utilizing the principle of protein-dye binding. *Anal Biochem* 1976; **72**: 255–260.
28 Fujita N *et al*. Targeted disruption of the mouse sphingolipid activator protein gene: a complex phenotype, including severe leukodystrophy and wide-spread storage of multiple sphingolipids. *Hum Mol Genet* 1996; **5**: 711–725.
29 Hahn CN *et al*. Generalized CNS disease and massive GM1-ganglioside accumulation in mice defective in lysosomal acid β-galactosidase. *Hum Mol Genet* 1997; **6**: 205–211.
30 Svennerholm L. Estimation of sialic acids. II. A colorimetric resorcinol-hydrochloric acid method. *Biochem Biophys Acta* 1957; **24**: 604–611.

J Hum Genet (2003) 48:571–574
DOI 10.1007/s10038-003-0080-9

ORIGINAL ARTICLE

Akemi Tanaka · Lan Thi Ngcok Hoang · Yasuaki Nishi
Satoshi Maniwa · Makio Oka · Tsunekazu Yamano

# Different attenuated phenotypes of GM2 gangliosidosis variant B in Japanese patients with *HEXA* mutations at codon 499, and five novel mutations responsible for infantile acute form

Received: 7 July 2003 / Accepted: 1 September 2003 / Published online: 18 October 2003


**Abstract** Eight mutations of the α subunit of β-hexosaminidase A gene (*HEXA*) were identified in eight patients with GM2 gangliosidosis variant B. They were five missense mutations, two splice-site mutations, and one two-base deletion. Five of them, R252L (CGT → CTT), N295S (AAT → AAC), W420C (TGG → TGT), IVS 13, +2A → C, and del 265–266AC (exon 2), were novel mutations responsible for infantile acute form of GM2 gangliosidosis. Two missense mutations, R499H and R499C, were found in one allele of two patients with attenuated phenotypes. The patient with R499C showed a late infantile form, and the other patient with R499H showed a juvenile form. These two mutations have been reported previously in the patients of other ethnic groups, and they have been known to cause attenuated phenotypes. The milder phenotypes of GM2 gangliosidosis variant B, different from the infantile acute form, have not been reported so far in Japan, and this is the first report of Japanese patients with attenuated phenotypes and their molecular analysis.

**Keywords** GM2 gangliosidosis · Tay-Sachs disease · Japanese · Infantile acute form · Late infantileform · Juvenile form

This work was supported by the Foundation of Osaka Fellowship (AT, 2001) from Osaka City, Japan, and the grant AT-11557060 from the Ministry of Education, Culture, Sports, Science and Technology of Japan.

A. Tanaka (✉) · L. T. N. Hoang · Y. Nishi · T. Yamano
Department of Pediatrics,
Osaka City University Graduate School of Medicine,
1-4-3 Asahi-machi, Abeno-ku,
Osaka 545-8585, Japan
E-mail: akemi-chan@med.osaka-cu.ac.jp
Tel.: +81-6-66453816
Fax: +81-6-66368737

S. Maniwa
Department of Pediatrics,
Matsuyama Red-Cross Hospital, Matsuyama, Japan

M. Oka
Department of Pediatrics,
Okayama University School of Medicine, Okayama, Japan

## Introduction

Tay-Sachs disease, GM2 gangliosidosis variant B, is an autosomal recessive disorder primarily affecting the central nervous system. It is caused by mutations in the gene encoding the α subunit of β-hexosaminidase A (Hex A), a lysosomal enzyme composed of α and β polypeptides. Hex A requires the assistance of GM2 activator protein for hydrolysis of the lipophilic ganglioside GM2 in the hydrophilic environment of the lysosome. Mutations in the β subunit and GM2 activator protein respectively result in the two other GM2 gangliosidoses known as Sandhoff disease (variant O) and activator protein deficiency (variant AB). Deficient catabolism and abnormal accumulation of ganglioside GM2 is a common feature in all GM2 gangliosidoses, and consequently they all exhibit similar clinical symptoms.

About hundred mutations in *HEXA* have been described in the literature (Gravel et al., 2001) so far. Some mutations are commonly found in ethnically or geographically isolated populations such as Ashkenazi Jewish patients (Myerowitz and Costigan, 1988; Arpaia et al., 1988; Myerowitz, 1988; Ohno and Suzuki, 1988) or French Canadian patients (Myerowitz and Hogikyan, 1986). We previously reported two common mutations among Japanese patients with Tay-Sachs disease. One was IVS 5, -1 G → T accounting for 80% of the mutant alleles (Tanaka et al., 1993) and the other was del nt613C accounting for 5% of the mutant alleles (Tanaka et al., 1999). Since both mutations result in null alleles and are responsible for infantile acute form of GM2 gangliosidosis, patients who show other clinical phenotypes than infantile

acute form have not been reported so far in the Japanese population.

We report here two patients with different attenuated clinical phenotypes of GM2 gangliosidosis caused by the different missense mutations in the same codon of *HEXA*. This is the first report of Japanese patients with attenuated phenotypes other than infantile acute form. In addition, we report five novel mutations responsible for infantile acute form of GM2 gangliosidosis variant B.

## Materials and methods

### Molecular and biochemical analysis

Cultured skin fibroblasts obtained from the patients with GM2 gangliosidosis variant B were used for the study in patients 1–6. Peripheral lymphocytes and chorionic villi were used in patients 7 and 8, respectively.

Genomic DNA was extracted from cells or tissue by the standard method. In the first step, two common mutations (IVS 5, -1 G → T and del nt613C) were screened by the previously reported method (Tanaka et al., 1999), and eight patients (patients 1–8) who had unknown mutations were selected. In the next step, PCRs and the sequencing were performed as described previously (Tanaka et al., 1999) to analyze the unknown mutations.

Enzyme analysis was carried out in the tissue homogenates with the substrates of 4-methylumbelliferyl-N-acetyl β-glucosaminide for the activity of hexosaminidase A plus B and 4-methylumbelliferyl-N-acetyl β-glucosamine-6-sulfate for the specific activity of hexosaminidase A according to the method of Suzuki (1987). All the patients gave their informed consent prior to their inclusion in this study.

### Patients' reports

Patients 1, 2, 3, 5, 7, and 8 showed the typical phenotype of infantile acute form of Tay-Sachs disease. The symptoms appeared at around 6 months of age. They never walked and became bedridden at about 1 year old. Patients 4 and 6 showed different attenuated phenotypes as described following. All patients had no records of consanguinities.

Patient 4, a 9-year-old boy: The patient developed normally until 1 year old when he could walk and speak one-word sentences. Mother noted that he showed no development after that, and consulted a doctor when he was 1 year and 6 months. The doctor found that he had hyperacusis and a cherry-red spot on the macula, and the diagnosis of GM2 gangliosidosis was made. He could not stand at age 2, and clonic seizures appeared at age 3. Nasal-tube feeding was introduced when he was 3. He was bed-ridden, had no social communications, and showed some myoclonic movements at the age of 7 years.

Patient 6, an 8-year-old girl: She developed normally until 3 years of age. She showed dysphemia at 3 years and 9 months. Then, she gradually lost words. She had the first attack of generalized seizure at 5 years and 10 months. Her EEG showed spike discharges at both temporal regions. The seizures appeared several times a day, and they were intractable by oral administration of anticonvulsants. She showed some difficulty with communication at 6 years and 5 months, nystagmus at 7 years and 1 month, and could not walk at 7 years and 2 months. At 7 years and 10 months, she was bed-ridden and showed some chorea-like involuntary movements. She could neither move nor communicate socially. She had no macular cherry-red spot. The brain MRI showed severe cortical atrophy. The diagnosis of GM2 gangliosidosis variant B was made by enzyme analysis.

## Results

The eight patients, who had unknown mutations in either of the two alleles, were selected by the screening of the two common mutations, as described previously. These patients were examined enzymatically and molecularly, and the results were summarized in Table 1. All except patient 1 had IVS 5, -1 G → T in one allele. Eight mutations were identified for 8 patients , which were five missense mutations, two splice-site mutations, and one two-base deletion. Five, R252L (CGT → CTT), N295S (AAT → AAC), W420C (TGG → TGT), IVS 13, +2A → C, and del 265–

**Table 1** Mutations in *HEXA* and hexosaminidase A (Hex A) activity in eight patients. Hex A activity was analyzed in the homogenate of cultured skin fibroblasts with 4-MU-N-acetyl β-glucosamine-6-sulfate as the substrate

| Patient | Phenotype | Allele 1 | Allele 2 | Hex-A activity |
|---|---|---|---|---|
| 1 | Infantile acute | IVS 3, +1G → T[a] | del 265, 266AC | 0.76 |
| 2 | Infantile acute | IVS 5, -1G → T[b] | IVS 13, +2A → C | 0.80 |
| 3 | Infantile acute | IVS 5, -1G → T[b] | W420C | 0.92 |
| 4 | Late infantile | IVS 5, -1G → T[b] | R499C[c] | 2.02 |
| 5 | Infantile acute | IVS 5, -1G → T[b] | R252L | 1.10 |
| 6 | Juvenile | IVS 5, -1G → T[b] | R499H[d] | 7.46 |
| 7 | Infantile acute | IVS 5, -1G → T[b] | IVS 6, +1G → A[e] | 4.94* |
| 8 | Infantile acute | IVS 5, -1G → T[b] | N295S | 2.05** |
| Homozygous patient ($n=10$) | Infantile acute | IVS 5, -1G → T[b] | IVS 5, -1G → T[b] | 1.14 ± 0.31 |
| Normal control | | | | |
| Fibroblast ($n=7$) | Normal | Wild | Wild | 582 ± 135 |
| Lymphocyte ($n=10$) | | | | 206 ± 37 |
| Cholionic villi ($n=10$) | | | | 396 ± 94 |

* Analyzed in the homogenate of peripheral lymphocytes
** Analyzed in the homogenate of chorionic villi. The activities are shown in nanomoles per milligrams per hour
[a] Mutation originally reported by Tanaka et al. (1994)
[b] Mutation originally reported by Tanaka et al. (1993)
[c] The same mutation was previously reported by Mules et al. (1992) and Akli et al. (1993)
[d] The same mutation was previously reported by Paw et al. (1990), Triggs-Raine et al. (1991), and Akli et al. (1993)
[e] The same mutation was previously reported by Akli et al. (1993)

266AC (exon 2), were novel mutations responsible for infantile acute form of GM2 gangliosidosis.

Two different missense mutations were found in the same codon in two patients (patients 4 and 6), R449C (CGT → TGT) and R449H (CGT → CAT), which caused the attenuated clinical phenotypes. Both mutations were generated at CpG spot. Patient 4 had R449C and showed late infantile form, and patient 6 had R449H and showed juvenile form. Hex A activity in these patients seemed to be higher than in other patients with infantile acute form, as shown in Table 1.

## Discussion

A huge number of mutations of *HEXA* gene have been reported previously. Most of them, about 90%, were known to cause the infantile acute form, so called Tay-Sachs disease, whose clinical phenotype is almost similar among patients from different ethnic groups. However, the clinical phenotypes of the chronic form are very heterogeneous (Gravel et al., 2001). Sometimes they show different phenotypes with the same mutation. The reason of this phenomenon is still unclear. Interactions between the mutant proteins from both alleles and the balance of those proteins must play an important role, which might be different among individuals even though they have the same mutations. Moreover, unknown effect from other genes or other proteins might occur.

GM2 gangliosidosis variant B in Japan is very unique. Most patients show infantile acute clinical phenotype and have the same mutation of IVS 5, -1G → T, which is considered to originate in Japan (Tanaka et al., 1994). Moreover, patients with milder forms have not been reported so far in the Japanese population.

We reported two Japanese patients with different attenuated phenotypes (late infantile and juvenile forms) and identified the disease-causing mutations in each patient. Both had the mutation of IVS 5, -1G → T in one allele. The mutations in another allele were R499C for one patient (patient 4) and R499H for the other (patient 6). Patient 4 showed a late infantile form, which was more severe than patient 6 but milder than other typical Japanese patients with GM2 gangliosidosis. Patient 6 showed a juvenile form.

Previously, R499C was reported in two patients—a French patient and an Italian patient—with infantile form (Akli et al., 1993), and one patient (Slavic/Irish) with adult form (Mules et al., 1992). R499H was reported in a Scottish/Irish patient (Paw et al., 1990) and a Scottish/English patient (Triggs-Raine et al., 1991) with juvenile form, and in a Dutch patient with adult form (Akli et al., 1993). All four, the two R499C patients with infantile form (a French patient and an Italian patient) and the two R499H patients with juvenile form (a Scottish/Irish patient and a Scottish/English patient), had the same null mutation of 4-base insertion in exon 11 in another allele. The molecular situation of the two patients in this report, who had R499C/H and a null mutation (IVS 5, -1G → T), is the same as these four patients with R499C/H and 4-base insertion. Patient 4 (R499C/IVS 5, -1G → T) showed less severe phenotype than the French and the Italian patients (R499C/4-base insertion). Patient 6 (R499H/IVS 5, -1G → T) showed a similar phenotype with the Scottish/Irish and the Scottish/English patients (R499H/4-base insertion).

The reason R499H causes mild phenotypes was previously studied biochemically (Paw et al., 1990). As the α-chain generated from the mutant allele with R499H would not be processed to the mature form, it would be unstable and unable to exit endoplasmic reticulum (ER). Some intracellular milieu might help to exit ER and to reach into lysosomes and create a small amount of mature polypeptide. In R499C, the cysteine residue might create an illegitimate disulfide bridge in the protein with a resultant disruption of the normal three-dimensional structure, causing a more severe clinical phenotype than in R499H (Akli et al., 1993). Our study of the structural analysis by molecular modeling software showed no drastic structural changes in α subunit polypeptides with R499C/H (Matsuzawa et al., 2003), which was consistent with the mild clinical phenotypes.

We also found six mutations in Japanese patients with infantile acute form. One, IVS 6, +1G → A, was reported previously in an American patient with subacute form (Akli et al., 1993). The remaining five mutations were novel. Two-base deletion (del 265, 266AC) would cause a flame shift and generate a stop signal at the 16th codon downstream to make a truncated polypeptide without biological function. As IVS 13, +2 A → C abolished the consensus sequence for the splicing, the mutation would cause impairment of normal splicing. W420C was reported previously in an Irish/German patient with infantile acute form. These two patients, this Irish/German patient and the patient in this report, had different nucleotide substitutions resulting in the same amino acid substitution, TGG to TGC and to TGT, respectively. R252L must be a disease-causing mutation because a different mutation in the same codon (R252H) was previously reported in a Portuguese patient (Ribeiro et al., 1996) who has mutation of B1 variant (a mutation for mild form) in another allele, and the amino acid R255 would be important for the protein structure. As N295 is one of the N-linked glycosylation sites of the α-chain polypeptide (Myerowitz et al., 1985), the amino acid substitution of N295S must cause a significant conformation change of the protein, which was consistent with the severe clinical phenotype of this patient.

**Acknowledgements** We thank the following doctors for providing the patients' materials: Kazuko Sukegawa at Gifu University (patient 1), Hitoshi Sakuraba at the Tokyo Metropolitan Institute of Medical Science (patient 2), Koji Inui at Osaka University (patients 3 and 5), Susumu Katayama (patient 4) and Yukitoshi Yamaguchi (patient 7) at Toho University, Tokyo, and Tsutomu Takahashi at Akita University (patient 8). We also thank Dr. Hitoshi Sakuraba

for the structural analysis of the mutant α subunit polypeptides by computer software.

## References


Akli S, Chomel J-C, Lacorte J-M, Bachner L, Poenaru L, Kahn A (1993) Ten novel mutations in the HEXA gene in non-Jewish Tay-Sachs patients. Hum Mol Genet 2:61–67

Arpaia E, Dumbrille-Ross A, Maler T, Neote K, Tropk M, Troxel C, Stirling JL, Pitts JS, Bapat B, Lamhonwah AM, Mahuran DJ, Schuster SM, Clarke JTR, Lowden JA, Gravel RA (1988) Identification of an altered splice site in Ashkenazi Tay-Sachs disease. Nature 333:85–86

Gravel RA, Kaback MM, Proia RL, Sandhoff K, Suzuki K, Suzuki Kuni (2001) The GM2 gangliosidoses. In: Scriver CR, Beaudet AL, Sly WS, Valle D, eds, the Metabolic and molecular bases of inherited disease, 8th edn. McGraw-Hill: New York, pp 3827–3876

Matsuzawa F, Aikawa S, Sakuraba H, Tanaka A, Hoang TNL, Ohno K, Ninomiya H, Sugimoto Y, Doi H (2003) Structural basis of the GM2 gangliosidosis B variant. J Hum Genet (in press) DOI 10.1007/s10038-003-0082-7

Mules EH, Hayflick S, Miller CS, Reynolds LW, Thomas GH (1992) Six novel deleterious and three neutral mutations in the gene encoding the α-subunit of hexosaminidase A in non-Jewish individuals. Am J Hum Genet 50:834–841

Myerowitz R (1988) Splice junction mutation in some Ashkenazi Jews with Tay-Sachs disease: Evidence against a single defect within this ethnic group. Proc Natl Acad Sci USA 85:3955–3959

Myerowitz R, Costigan FC (1988) The major defect in Ashkenazi Jews with Tay-Sachs disease is an insertion in the gene for the α-chain of β-hexosaminidase. J Biol Chem 263:18587–18589

Myerowitz R, Hogikyan ND (1986) A deletion involving alu sequences in the β-hexosaminidase α-chain gene of French Canadians with Tay-Sachs disease. J Biol Chem 262:15396–15399

Myerowitz R, Piekarz R, Neufeld EF, Shows TB, Suzuki K (1985) Human β-hexosaminidase α chain: Cloning sequence and homology with the β chain. Proc Natl Acad Sci USA 82:7830–7834

Ohno K, Suzuki K (1988) A splicing defect due to an exon-intron junctional mutation results in abnormal β-hexosaminidase α chain mRNAs in Ashkenazi Jewish patients with Tay-Sachs disease. Biochem Biophys Res Commun 153:463–469

Paw BH, Moskowitz SM, Uhrhammer N, Wright N, kaback MK, Neufeld EF (1990) Juvenile GM2 gangliosidosis caused by substitution of histidine for arginine at position 499 or 504 of the α-subunit of β-hexosaminidase. J Biol Chem 265:9452–9457

Ribeiro MG, Sonin T, Pinto RA, Fontes A, Ribiero H, Pinto E, Palmeira MM, Sa Miranda MC (1996) Clinical, enzymatic, and molecular characterization of a Portuguese family with a chronic form of GM2-gangliosidosis B1 variant. J Med Genet 33:341–343

Suzuki K (1987) Enzymatic diagnosis of sphingolipidosis. Methods Enzymol 138:727–762

Tanaka A, Sakuraba H, Isshiki G, Suzuki K (1993) The major mutation among Japanese patients with infantile Tay-Sachs disease: A G-to-T transversion at the acceptor site of intron 5 of the β-hexosaminidase α gene. Biochem Biophys Res Comm 192:539–546

Tanaka A, Sakazaki H, Murakami H, Isshiki G, Suzuki K (1994) Molecular genetics of Tay-Sachs disease in Japan. J Inher Metab Dis 17:593–600

Tanaka A, Fujimaru M, Choeh K, Isshiki G (1999) Novel mutations including the second most common in Japan in the β-hexosaminidase α subunit gene, and a simple screening of Japanese patients with Tay-Sachs disease. J Hum Genet 44:91–95

Triggs-Raine BL, Akerman BR, Clarke JTR, Gravel RA (1991) Sequence of DNA flanking the exons of the HEXA gene, and identification of mutations in Tay-Sachs disease. Am J Hum Genet 49:1041–1054

ELSEVIER

# Magnetic Resonance Imaging in Occipital Lobe Epilepsy with Frequent Seizures

Hideji Hattori, MD, Osamu Matsuoka, MD, Hiroshi Ishida, MD, Saeri Hisatsune, MD, and Tsunekazu Yamano, MD

**Magnetic resonance imaging and single-photon emission computed tomography provide useful information in the evaluation of the pathophysiology of epileptic foci. Ictal magnetic resonance imaging in a 7-year-old male with occipital lobe epilepsy revealed mild swelling of the left temporo-occipital region, with hyperintensity on $T_2$-weighted and fluid attenuated inversion recovery images. This lesion, however, was not detected on diffusion-weighted imaging. An ictal single-photon emission computed tomography study using 99mTc-ECD demonstrated left temporo-occipital hyperperfusion. $T_2$-weighted and fluid attenuated inversion recovery images revealed hyperintensity without atrophy 4 months after control of his seizures. The focus in nonconvulsive status epilepticus has been reported as showing hyperintensity on $T_2$-weighted, fluid attenuated inversion recovery and diffusion-weighted images. Since hyperintensity on diffusion-weighted imaging reflects cytotoxic intracellular edema due to excitotoxicity, and his ictal diffusion-weighted image exhibited no remarkable change, the lesions in the left temporo-occipital region resulted from vasogenic edema. Cytotoxic edema resulting from excitotoxicity leads to neuronal death, causing cortical atrophy. Thus, diffusion-weighted imaging is a useful tool to predict the prognosis of frequent seizures.** © 2003 by Elsevier Inc. All rights reserved.

Hattori H, Matsuoka O, Ishida H, Hisatsune S, Yamano T. Magnetic resonance imaging in occipital lobe epilepsy with frequent seizures. Pediatr Neurol 2003;28:216-218.

## Introduction

There have been a number of studies concerning the pathogenesis of epilepsy using experimental animals. They have offered valuable information to help understand the pathophysiology of human epilepsy. Neuroimaging using magnetic resonance imaging (MRI) and single-photon emission computed tomography (SPECT) also has contributed to evaluating the pathophysiology of the patient with localization-related epilepsy [1-6]. We present a male with occipital lobe epilepsy, who suffered from frequent seizures, whose ictal MRI and SPECT helped us to elucidate the pathophysiology of his epileptic focus.

## Case Report

The male was delivered at 41 weeks gestation by cesarean section for placenta previa. He was the mother's first child. She had suffered from occasional complex partial seizures 1 year before the pregnancy and had taken antiepileptic drugs while pregnant. The amniotic fluid was slightly turbid. Birth weight was 3,750 g, length 51.5 cm, and head circumference 35 cm. Apgar scores at 1 and 5 minutes were 6 and 9, respectively. His developmental milestones were normal. He had his first seizure while watching television when he was 7 years old. The seizure involved transient nausea and headache with a sensation of glare. He had rapid, abnormal eye movement. The episode lasted less than 30 seconds. The seizures became increasingly frequent and were sometimes associated with loss of consciousness and tonic posturing while walking. Postictally he sometimes complained of fear, transient blindness, and visual disturbance such as the perception of rotation of his mother's face. He was admitted to our hospital.

On admission, he was having 20 to 30 seizures per day. His neurologic examination was unremarkable. He underwent electroencephalogram (EEG) examination, brain MRI, and SPECT. Interictal EEG revealed continuous high-voltage slow wave bursts in the left occipital region and spikes at the right central region on awakening. Seizure activity was not induced by photic stimulation or sleep. Video-EEG recording during the ictal state revealed rhythmic 2-2.5 Hz high voltage slow waves starting in the bilateral frontal region that were associated with nystagmus. Subsequently, 20-25 Hz rhythms increasing in amplitude appeared at the left occipital region, spreading to the left temporo-parietal region. MRI demonstrated mild swelling of the left temporo-occipital region, which revealed signal hyperintensity on $T_2$-weighted and fluid attenuated inversion recovery (FLAIR) images (Figs 1A,B). This lesion was not detected by diffusion-weighted image (DWI) (Fig 1C). MRI also demonstrated mild dilatation of the posterior horn of the left lateral ventricle. Although we suspected this change might be the residue of old brain damage, the exact etiology was unclear. Ictal SPECT study using 99mTc-ECD revealed left temporo-occipital hyperperfusion (Fig 1D).

Clinical manifestations and the EEG findings caused us to diagnose occipital lobe epilepsy, and carbamazepine (CBZ) was prescribed. CBZ was gradually increased in dosage from 3 mg/kg/day to 10 mg/kg/day in

From the Department of Pediatrics, Osaka City University Graduate School of Medicine, Osaka, Japan.

Communications should be addressed to:
Dr. Hattori; Department of Pediatrics; Osaka City University Graduate School of Medicine; 1-4-3, Asahi-machi, Abeno-ku; Osaka, 545-8585, Japan.
Received May 7, 2002; accepted September 16, 2002.




doi:10.1016/S0887-8994(02)00615-X • 0887-8994/03/$—see front matter

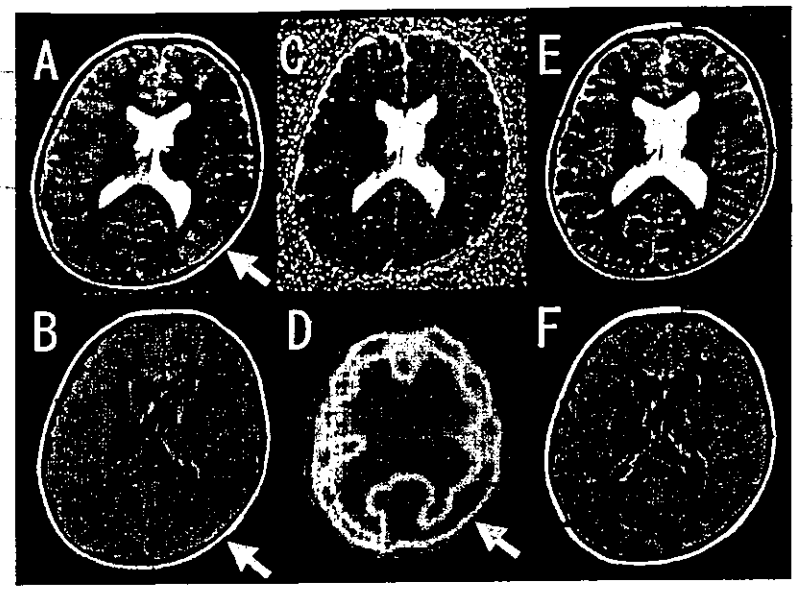


*Figure 1. MRI revealed signal hyperintensity by $T_2$-weighted (A) and FLAIR (B) images in the left temporo-occipital region. DWI of MRI did not demonstrate abnormal intensity area (C). Simultaneously examined SPECT showed hyperperfusion in the left temporo-occipital cortex (D). The 4-month follow-up MRI exhibited no signal abnormality or cortical atrophy by $T_2$-weighted (E) and FLAIR (F) images. Both MRIs demonstrated mild dilatation of the posterior horn of the left lateral ventricle. (A) $T_2$-weighted image: Fast spin echo, TR/TE 4000/107 msec, (B) FLAIR image: TR/TE/TI 9002/150/2200 msec, (C) DWI: apparent diffusion constant (ADC) image, TR/TE 5000, 102.5 msec, b value=600, 800, 1000, (E) $T_2$-weighted image: Fast spin echo, TR/TE 4000/102 msec, (F) FLAIR image: TR/TE/TI 10002/172/2200 msec. TR: repetition time, TE: echo time, TI: inversion time.*

12 days. The serum concentration of CBZ reached 6.5 to 7. μg/ml. Acetazolamide (250 mg/day) was added to CBZ from 14 to 27 hospital days, when signal hyperintensity by $T_2$-weighted images in the left temporo-occipital region resolved. As seizure activity persisted, CBZ was increased to 12 mg/kg/day. The seizures decreased in frequency and subsided completely by 32 days. At this time, SPECT revealed mild left temporo-occipital hypoperfusion. Although MRI after 4 months of seizure control demonstrated mild dilatation of the posterior horn of the left lateral ventricle, it did not reveal any abnormalities such as cortical atrophy or hyperintensity on $T_2$-weighted and FLAIR images in the left temporo-occipital area (Fig 1 E,F). The patient had no neurologic sequelae.

## Discussion

There have been several studies concerning MRI and SPECT findings in localization-related status epilepticus [1-6]. They reported that hyperintense signals in $T_2$-weighted and FLAIR images were observed in both hippocampal and neocortical tissues [1-3]. Chu et al. described that DWI also revealed diffuse gyriform cortical hyperintensity throughout the brain in nonconvulsive status epilepticus [7]. It was known that ictal SPECT demonstrated hyperperfusion at the epileptic focus. Our patient suffered from frequent nonconvulsive seizures but did not fit the definition of being in status epilepticus. His initial MRI study exhibited swelling and hyperintensity of the left temporo-occipital area in $T_2$-weighted and FLAIR images, but did not reveal any abnormal signal on DWI.

Generally, hyperintensity on $T_2$-weighted and FLAIR images reflects vasogenic extracellular edema and/or cytotoxic intracellular edema, whereas hyperintensity on DWI indicates only cytotoxic intracellular edema [7-8]. Thus, the MRI findings in our case revealed that the frequent seizures induced vasogenic extracellular edema, but did not cause neuronal cytotoxic intracellular edema in the temporo-occipital region.

MRI findings regarding the epileptic focus in the ictal state may be divided into three types according to the intensity of seizures, (i.e., no significant findings, signal hyperintensity on $T_2$-weighted and FLAIR images, and signal hyperintensity on $T_2$-weighted, FLAIR and additional diffusion weighted images, respectively). Pathophysiologically, hyperperfusion, vasogenic extracellular edema, and then cytotoxic intracellular edema may be chronologically induced in the epileptic focus in proportion to the intensity of seizures.

The lesions demonstrating hyperintensity by DWI are reported to result in gliosis with atrophy. In our case an MRI examined after 4 months of seizure control did not reveal any atrophy of the epileptic focus, and the patient did not have any neurologic sequelae. Vasogenic edema is thought to depend on altered permeability of the vessels in relation to frequent seizures, resulting in fluid accumulation in the extracellular space [3]. The results obtained from our patient indicate that vasogenic edema is repaired without neurologic sequelae, if seizures do not develop into status epilepticus. In status epilepticus, cytotoxic edema is induced due to excitotoxicity, leading to neuronal death, causing brain atrophy. Thus, DWI MRI imaging is a useful tool to predict prognosis in patients with frequent seizures.

### References

[1] **Meierkord** H, Wieshmann U, Niehaus L, Lehmann R. Structural consequences of status epilepticus demonstrated with serial magnetic resonance imaging. Acta Neurol Scand 1997;96:127-32.

[2] **Lansberg** MG, O'Brien MW, Norbash AM, Moseley ME, Morrell M, Albers GW. MRI abnormalities associated with partial status epilepticus. Neurology 1999;52:1021-7.

[3] **Lazeyras** F, Blanke O, Zimine I, Delavelle J, Perrig SH, Seeck M. MRI, 1H-MRS and functional MRI during and after prolonged nonconvulsive seizure activity. Neurology 2000;55:1677-82.

[4] **Hollo** A, Kaminska A, Vera P, et al. Ictal perfusion changes during occipital seizures in infancy: Report of two serial ictal observations. Epilepsia 2001;42:275-9.

[5] Sturm JW, Newton MR, Chinvarun Y, Berlangieri SU, Berkovic SF. Ictal SPECT and interictal PET in the localization of occipital lobe epilepsy. Epilepsia 2000;41:463-6.

[6] Kim SK, Lee DS, Lee SK, et al. Diagnostic performance of [18F] FDG-PET and ictal [99mTc]-HMPAO SPECT in occipital lobe epilepsy. Epilepsia 2001;42:1531-40.

[7] Chu K, Kang DW, Kim JY, Chang KH, Lee SK. Diffusion-weighted magnetic resonance imaging in nonconvulsive status epilepticus. Arch Neurol 2001;58:993-8.

[8] Chu K, Kang DW, Kim HJ, Lee YS, Park SH. Diffusion-weighted imaging abnormalities in Wernicke encephalopathy: Reversible cytotoxic edema? Arch Neurol 2002;59:123-7.

JOURNAL OF BONE AND MINERAL RESEARCH
Volume 18, Number 11, 2003


# Regulatory Mechanisms and Physiological Relevance of a Voltage-Gated $H^+$ Channel in Murine Osteoclasts: Phorbol Myristate Acetate Induces Cell Acidosis and the Channel Activation

HIROYUKI MORI,[1] HIROMU SAKAI,[1] HIROKAZU MORIHATA,[1] JUNKO KAWAWAKI,[2] HITOSHI AMANO,[3] TSUNEKAZU YAMANO,[4] and MIYUKI KUNO[1]

## ABSTRACT

**The voltage-gated $H^+$ channel is a powerful $H^+$ extruding mechanism of osteoclasts, but its functional roles and regulatory mechanisms remain unclear. Electrophysiological recordings revealed that the $H^+$ channel operated on activation of protein kinase C together with cell acidosis.**

**Introduction:** $H^+$ is a key signaling ion in bone resorption. In addition to $H^+$ pumps and exchangers, osteoclasts are equipped with $H^+$ conductive pathways to compensate rapidly for pH imbalance. The $H^+$ channel is distinct in its strong $H^+$ extrusion ability and voltage-dependent gatings.

**Methods:** To investigate how and when the $H^+$ channel is available in functional osteoclasts, the effects of phorbol 12-myristate 13-acetate (PMA), an activator for protein kinase C, on the $H^+$ channel were examined in murine osteoclasts generated in the presence of soluble RANKL (sRANKL) and macrophage-colony stimulating factor (M-CSF).

**Results and Conclusions:** Whole cell recordings clearly showed that the $H^+$ current was enhanced by increasing the pH gradient across the plasma membrane ($\Delta$pH), indicating that the $H^+$ channel changed its activity by sensing $\Delta$pH. The reversal potential ($V_{rev}$) was a valuable tool for the real-time monitoring of $\Delta$pH in clamped cells. In the permeabilized patch, PMA (10 nM–1.6 $\mu$M) increased the current density and the activation rate, slowed decay of tail currents, and shifted the threshold toward more negative voltages. In addition, PMA caused a negative shift of $V_{rev}$, suggesting that intracellular acidification occurred. The PMA-induced cell acidosis was confirmed using a fluorescent pH indicator (BCECF), which recovered quickly in a $K^+$-rich alkaline solution, probably through the activated $H^+$ channel. Both cell acidosis and activation of the $H^+$ channel by PMA were inhibited by staurosporine. In ~80% of cells, the PMA-induced augmentation in the current activity remained after compensating for the $\Delta$pH changes, implying that both $\Delta$pH-dependent and -independent mechanisms mediated the channel activation. Activation of the $H^+$ channel shifted the membrane potential toward $V_{rev}$. These data suggest that the $H^+$ channel may contribute to regulation of the pH environments and the membrane potential in osteoclasts activated by protein kinase C.

**J Bone Miner Res 2003;18:2069–2076**

**Key words: osteoclast, proton channel, cell acidosis, pH homeostasis, phorbol ester**

## INTRODUCTION

DIVERSE $H^+$-TRANSLOCATING MECHANISMS are involved in regulation of osteoclast functions.[1] The vacuolar-type $H^+$-ATPase (V-ATPase) in the ruffled membrane may be the primary mechanism responsible for $H^+$ secretion into the resorption pit formed between osteoclasts and the bone surface. $Na^+$-$H^+$ exchangers are ubiquitous regulators for intracellular pH ($pH_i$). Voltage-gated $H^+$ channels, which are $H^+$ conductive pathways, are expressed in many types of macrophage-lineage cells including macrophages,[2,3] microglia,[4,5] and osteoclasts.[6,7] $H^+$ channels are distinct in

The authors have no conflict of interest.

[1]Department of Physiology, Osaka City University Graduate School of Medicine, Osaka, Japan.
[2]Central Laboratory, Osaka City University Graduate School of Medicine, Osaka, Japan.
[3]Department of Pharmacology, School of Dentistry, Showa University, Tokyo, Japan.
[4]Department of Pediatrics, Osaka City University Graduate School of Medicine, Osaka, Japan.

their surprisingly high $H^+$ extrusion rate, ~100 times as strong as the pumps and exchangers, and have been hypothesized to compensate rapidly for pH imbalance across the plasma membrane.[8] However, their physiological or pathological relevance to osteoclast functions remains unclear because there has been no information about the channel activity under possible functional states. Clarifying how and when the $H^+$ channel is activated is crucial to understanding the functional roles of the channel, which may provide a new insight into the $H^+$ signaling system of osteoclasts.

The $H^+$ channels are characterized by an extremely high selectivity for $H^+$ (>$10^6$ times more permeable to $H^+$ than to other ions), voltage- and time-dependent gating, strong outward rectification, and blockage by $Zn^{2+}$. There is not yet consensus on the molecular identity of the channel,[9] but it is considered to be a molecule with a distinct and unidentified permeation mechanism.[8] The $H^+$ channel activity is dynamic and responsive to changes in cell conditions, such as, temperature,[10,11] cell swelling,[5] intracellular $Ca^{2+}$,[3] actions of NADPH oxidases,[12–14] and phorbol esters.[12,14–17] Phorbol esters enhance bone resorption by modifying various osteoclastic activities, such as organization of the cytoskeletal network, $[Ca^{2+}]_o$-sensing responses, increases in calmodulin, and downregulation of CSF-1 binding sites.[18–21] In this study, to reveal conditions under which the $H^+$ channel is available in osteoclasts, we investigated the effects of phorbol ester on the channel activity. A preliminary account has been made.[22]

## MATERIALS AND METHODS

### *Cells*

Osteoclasts were generated from murine bone marrow cells in the presence of macrophage-colony stimulating factor-1 (M-CSF-1; Peprotec, London, UK) and a soluble form of RANKL (sRANKL; Peprotec).[23,24] After male, 5 to 8-week-old, C3H/HeN mice were killed by cervical dislocation, bone marrow cells were obtained from the tibias and femurs, centrifuged at 700*g* for 7 minutes at 4°C, and suspended in 1 ml of α-MEM supplemented with 15% fetal calf serum (FCS), 0.1 mg/ml streptomycin, and 100 U/ml penicillin. The cell suspension was placed on a chromatography column filled with 5 ml of Sephadex G10 gel (Amersham Pharmacia Biotech, Buckinghamshire, UK) and was incubated at 37°C in a 95% air-5% $CO_2$ atmosphere for 45 minutes. After removing adherent cells by means of gel filtration, nonadherent cells were centrifuged at 700*g* for 7 minutes at 4°C and plated on glass coverslips at $2 \times 10^7$ cells/ml in the fresh medium containing 10–20 ng/ml M-CSF and 50–100 ng/ml sRANKL. Cells were fed on the coverslips coated with M-CSF and/or RANKL. One-half of the medium was changed every 2 days. Multinuclear cells appeared within 5 days in culture and were maintained for 10–15 days. Osteoclasts were identified with the phase-contrast microscopy as multinucleated cells with TRACP activity.[25]

### *Solutions*

In whole cell recordings, the external solution contained (mM) 75 *N*-methyl D-glucamine (NMDG) aspartate, 1 $CaCl_2$, 1 $MgCl_2$, 10 glucose, 80–100 HEPES (pH = 6.8–7.8), and 0.1% bovine serum albumin (BSA). Generally, 100 μM of 4,4′-diisothiocyanato-2,2′-stilbene sulfonate (DIDS) was added to the bath to block $Cl^-$ channels.[7,25] The pipette solutions contained (in mM) 65 NMDG aspartate or 75 Cs-methanesulfonate, 3 $MgCl_2$, 1 BAPTA, 5 $Na_2ATP$, 120 Mes, or 100 HEPES (pH = 5.5–7.8). The buffers, Mes and HEPES, were used to make the pipette solutions of $pH_p$ < 7.0 and ≥7.0, respectively. The pH of the bath and pipette solutions ($pH_o$ and $pH_p$) was adjusted by CsOH. Osmolality of the solutions was maintained between 280 and 300 mOsm. In the permeabilized-patch recordings, the same pipette and bath solutions were used: $pH_o$ was maintained at 7.3 unless described otherwise. Amphotericin B (~500 μg/ml) was added to the pipette solutions. As $pH_p$ could not control intracellular pH, there was no significant difference in the reversal potential for the $H^+$ current ($V_{rev}$) and the $H^+$ current density under different $pH_p$: $V_{rev}$ and the current density measured at the end of 2-s-long depolarization (100 mV) were 23 ± 4 mV ($n$ = 41) and 4.4 ± 0.8 pA/pF ($n$ = 39) at $pH_p$ 5.5 and 19 ± 4 mV ($n$ = 14) and 3.4 ± 0.4 pA/pF ($n$ = 18) at 7.3–7.6. However, in some cases, the current increased with a shift in $V_{rev}$ before stimulation. We discarded these cases where effects of $pH_p$ could not be excluded. To evaluate $H^+$ channel activities under more physiological conditions, the bath contained standard Ringer solution (in mM) 145 NaCl, 5 KCl, 1 $CaCl_2$, 1 $MgCl_2$, and 10 HEPES (pH 7.3), and the pipette contained (in mM) 150 K-gluconate, 3 $MgCl_2$, 1 EGTA, and 10 HEPES (pH 7.3).

### *Electrophysiological recordings*

Currents were recorded from osteoclasts at room temperature (20–24°C). The borosilicate glass pipettes had a resistance of 5–8 MΩ. The series resistance compensation (60–80%) was conducted to reduce the voltage error. The reference electrode was an Ag-AgCl wire connected to the bath solution through a Ringer-agar bridge. The zero current potential before formation of the gigaseal (1–5 GΩ) was taken as 0 mV. The $H^+$ current developed gradually in the permeabilized patch, usually for 10–20 minutes. Data were obtained after the current activity and $V_{rev}$ were stabilized. Current signals were recorded with an amplifier (Axopatch 200A; Axon Instruments, Foster City, CA, USA), digitized at 1–2 kHz with an analog-digital converter (Digidata 1200; Axon Instruments), and analyzed using pCLAMP software (Axon Instruments). Voltage steps were applied at a holding potential of −60 mV every 10–60 s. The interval of stimulation was determined to minimize decreases in ΔpH caused by the preceding $H^+$ efflux.[7,26] Leak current was estimated from the linear portion of the current-voltage ($I$-$V$) relation when either inward or outward current was absent or eliminated by the blockers. After subtracting leak currents, data were expressed as means ± SE. Statistical significance ($p < 0.05$) was tested using unpaired Student's $t$-test unless stated otherwise.

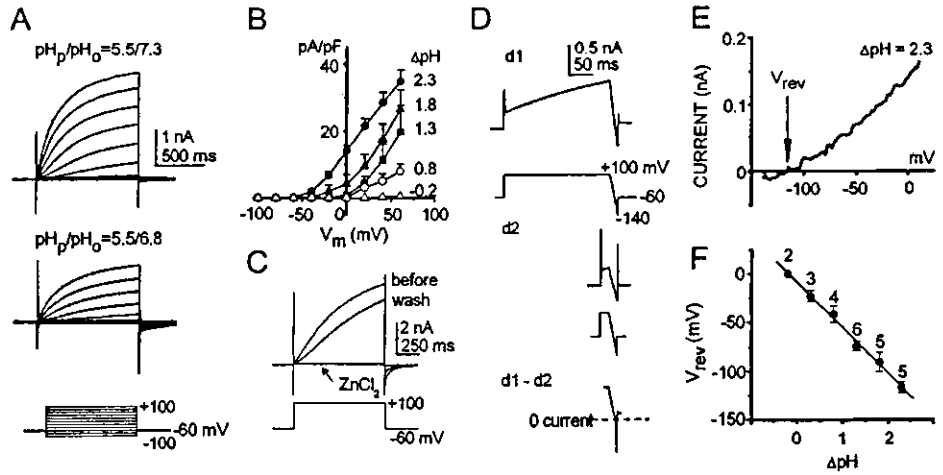


FIG. 1. Whole cell, voltage-gated $H^+$ currents in murine osteoclasts. (A) $H^+$ currents evoked by voltage steps applied at −60 mV. (B) Current-voltage (*I-V*) relationships under different ΔpH ($pH_o$ − $pH_p$). The current amplitude was measured at the end of 1-s-long voltage steps, normalized by cell capacitance, and was plotted against the membrane potential ($V_m$). Data (means ± SE) were obtained at $pH_p/pH_o$ of 5.5/7.8 ($n$ = 4), 5.5/7.3 ($n$ = 13), 5.5/6.8 ($n$ = 4), 7.0/7.8 ($n$ = 5), and 7.0/6.8 ($n$ = 2). (C) $Zn^{2+}$ (100 μM) blocked the current reversibly. (D) $H^+$ currents recorded with a ramp-repolarization method. A 20-ms-long repolarizing voltage ramp from + 100 to −140 mV was applied following 250 ms- (d1) or 20-ms-long (d2) prepotentials (+100 mV). (E) The *I-V* relation of the subtracted current ($pH_p/pH_o$ = 5.5/7.8). An arrow indicates the reversal potential ($V_{rev}$). (F) $V_{rev}$ plotted against ΔpH. The line represents a least square's fit for the data ($r$ = 0.99). In A–F, the bath contained NMDG aspartate and 100 μM DIDS. The pipette contained Cs-methanesulfonate.

Osteoclasts were stimulated by perfusing the bath solution containing PMA at about 0.1 ml/s (volume of the recording chamber; 2 ml). This perfusion was often accompanied by transient increase in temperature by 1–2°C. Because the $H^+$ channel has a strong temperature sensitivity,[10,11] the effects of PMA were analyzed after temperature returned to that before the perfusions.

### *Measurements of intracellular pH using 2',7'-bis-(2-carboxyethyl)-5 (and -6) carboxyfluorescein*

$pH_i$ of single nonclamped cells was determined with a digital fluorescence microscopy (Attofluor; Atto Bioscience, Rockville, MD, USA) using a pH-sensitive fluorescent dye, 2',7'-bis-(2-carboxyethyl)-5 (and -6) carboxyfluorescein (BCECF). Cells were loaded with the acetoxymethyl ester form of BCECF (BCECF-AM; 2–5 μM) for 30 minutes at 37°C. After washing the dye, the ratios of fluorescent images (emission wavelength ≥ 520 nm) excited at two wave lengths (488 and 460 nm) were measured every 20 s with 30- to 100-ms exposures. Data (80–120 pixels for each cell) for each illumination were averaged and plotted against time. Calibration of $pH_i$ was carried out by dissipating ΔpH with 10 μM nigericin in a $K^+$-rich solution with known pH values.[5]

### *Chemicals*

Mes, BAPTA, and BCECF-AM were purchased from Dojindo Laboratories (Kumamoto, Japan). All other chemicals were obtained from Sigma Chemical Co. (St Louis, MO, USA). A condensed stock solution of $Na_2ATP$ (500 mM) was prepared in 1 M Tris-Cl, stored in a freezer, and added to the internal medium before use. Stock solutions of PMA, DIDS, and diphenylene iodinium (DPI) were dissolved in dimethyl sulfoxide (DMSO) and nigericin in ethanol. The final concentration of DMSO (≤0.1%) or ethanol (≤1%) did not affect the membrane currents.

## RESULTS

### *Voltage-gated $H^+$ currents in murine osteoclasts*

Figure 1A shows whole cell recordings of voltage-gated $H^+$ currents in murine osteoclasts when other ion currents were eliminated. The $H^+$ currents were characterized by activation on depolarization, slow activation kinetics, and outward rectification.[7] The current amplitude and the activation rate were reduced by decreasing $pH_o$. The current-voltage (*I-V*) relationships for the current density obtained under various combinations of $pH_p$ and $pH_o$ showed that increases in the ΔpH shifted the curve to more negative voltages (Fig. 1B). The membrane potential was designated as $V_m$. The $H^+$ current was reversibly blocked by $ZnCl_2$ (Fig. 1C).

The reversal potential ($V_{rev}$) for the $H^+$ current was determined by a ramp-repolarization method (Fig. 1D)[7,27]: repolarization voltage ramps were applied following long (d1) and short (d2) depolarizations. The latter protocol generated only capacitative and leak currents, because open $H^+$ channels may be few during the period. Subtraction (d1 − d2) yielded the net current flowing through the channel during the voltage ramp. $V_{rev}$, indicated by the zero-current potential of the *I-V* curve for the net current (Fig. 1E, arrow), had a linear correlation to ΔpH with a slope of 47 mV per ΔpH of 1 (Fig. 1F). Because concentrations of ions other than $H^+$ changed little during the measurements, the $H^+$ ion was the major carrier for the current.[8] Thus, $V_{rev}$ was a valuable tool for real-time monitoring ΔpH in clamped cells.

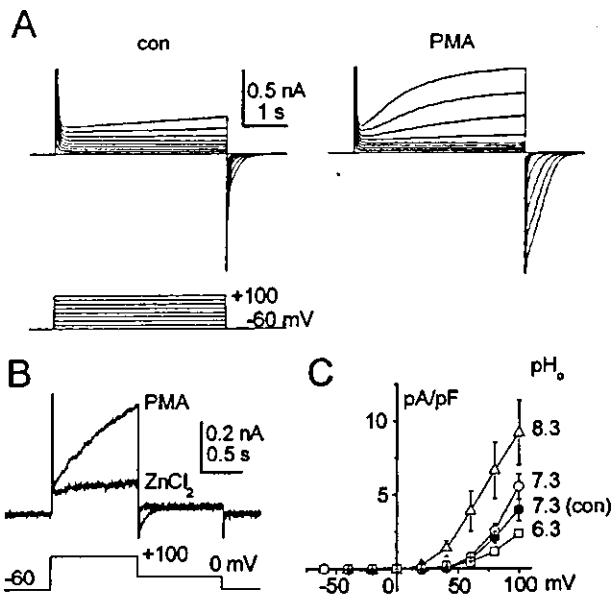


FIG. 2. PMA-activated $H^+$ currents in the permeabilized patch. (A) $H^+$ currents at various potentials before and after stimulation with PMA (1.6 $\mu$M) in a permeabilized patch. The bath contained NMDG aspartate and 100 $\mu$M DIDS. The pipette contained Cs-methanesulfonate. $pH_p/pH_o$ = 5.5/7.3. (B) $Zn^{2+}$ (100 $\mu$M) blocked both outward and inward currents activated by PMA (1 $\mu$M). (C) Mean *I-V* relationships before (con) and after addition of PMA (1 $\mu$M) obtained from three cells. The current amplitude was measured at the end of 2-s-long voltage steps. $pH_o$ was 7.3 and then changed to 8.3 ($n$ = 3) and 6.3 ($n$ = 2). B and C were obtained with the bath and pipette solutions of physiological compositions ($pH_p/pH_o$ = 7.3/7.3).

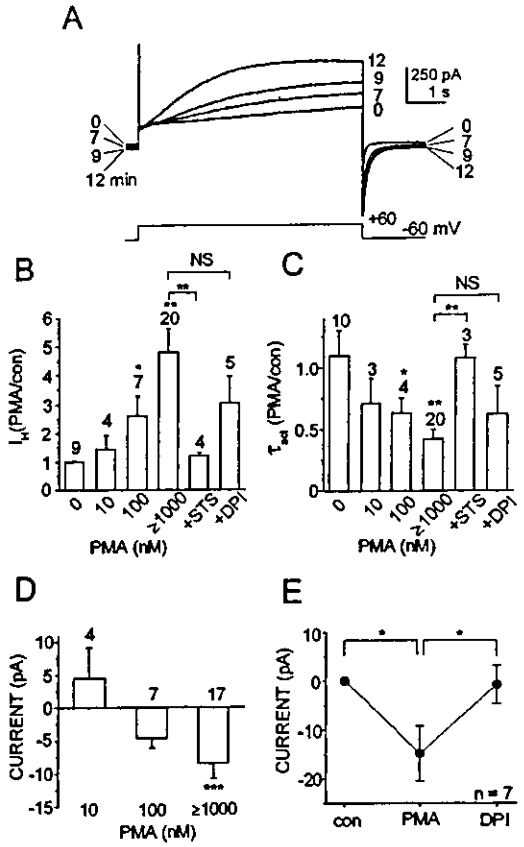


FIG. 3. PMA-induced activation of the $H^+$ currents and electron currents. (A) $H^+$ currents at 0, 7, 9, and 12 min after addition of 1.6 $\mu$M PMA in the permeabilized patch. Inward currents were also generated at −60 mV. (B and C) PMA-induced changes in the (B) current density and (C) $\tau_{act}$ obtained from the currents evoked by 2- to 8-s-long depolarization steps (+40–100 mV) in 3–20 cells. The data (means ± SE) represent the maximal ratio to the controls within 10–15 min after stimulation: ≥1000 represents 1000–1600 nM. Staurosporine (1 $\mu$M) or DPI (10 $\mu$M) were coapplied with 1 $\mu$M PMA. (D) PMA-induced currents at −60 mV. (E) currents at −60 mV in seven cells that were perfused with the PMA (1 $\mu$M)- and DPI-containing solutions sequentially. Zero indicates the current level before stimulation. $*p < 0.05$, $**p < 0.01$, and $***p < 0.001$ compared with the values with no PMA. In E, $*p < 0.05$ with paired $t$-test. The bath contained NMDG aspartate and 100 $\mu$M DIDS. The pipette contained Cs-methanesulfonate. $pH_p/pH_o$ = 5.5–7.6/7.3.

### *PMA-induced potentiation of the $H^+$ current*

In the whole cell recordings, the effects of PMA on the $H^+$ current were inconsistent and small, if any. Therefore, the permeabilized patch was used in further experiments to preserve the cell machinery required for activating PKC.[14] In addition, $pH_i$ was not controlled by pH-buffer molecules in the pipette, because HEPES or Mes might be too large to pass through amphotericin pores (see the Materials and Methods section). This allowed $pH_i$ to change under actions of intrinsic buffers. Application of PMA enhanced the $H^+$ current in the permeabilized patch (Fig. 2A). The activated currents shared the same electrophysiological properties with the whole cell $H^+$ currents, such as voltage- and time-dependent activation, outward rectification, blockade by $ZnCl_2$ (Fig. 2B), and pH dependence (Fig. 2C). Inward tail currents, decay of which was slowed by PMA (Fig. 2A), were also sensitive to $Zn^{2+}$ (Fig. 2B). Figures 2B and 2C were recorded from cells bathed in the standard Ringer solution with a $K^+$-rich pipette solution without DIDS, indicating that PMA activated the $H^+$ current under the physiological condition as well. The control current density measured at the end of a 2-s-long depolarization (100 mV) was 4.32 ± 0.32 pA/pF ($n$ = 11) in the physiological conditions, which was not significantly different from that in the solutions eliminating $K^+$ and $Cl^-$ (3.72 ± 0.59 pA/pF, $n$ = 26). In some cells, the $H^+$ current was contaminated with outward $Cl^-$ or $K^+$ currents. Thus, in later experiments, the effects of PMA on the $H^+$ current were examined in the absence of other channels unless described otherwise.

The current amplitude and the activation rate began to increase within 5 minutes after stimulation with PMA (Fig. 3A). The potentiation of the $H^+$ current lasted for >10–20 minutes and seldom reversed spontaneously. Figures 3B and 3C summarize the maximal effects of PMA on the current density and the activation time constant ($\tau_{act}$) within 10–15 minutes of exposure to PMA. The current density was increased by a factor of 1.4 ± 0.5 ($n$ = 4) at 10 nM PMA, 2.6 ± 0.7 ($n$ = 7) at 100 nM, and 4.8 ± 0.8 ($n$ = 20) at 1–1.6 $\mu$M. Decreases in the $\tau_{act}$ by PMA were also dose-dependent (0.71 ± 0.20 for 10 nM, $n$ = 3; 0.63 ± 0.12 for 100 nM, $n$ = 4; 0.42 ± 0.08 for 1–1.6 $\mu$M, $n$ = 20). The

pH of the pipette solutions did not affect these values significantly, suggesting that the PMA-induced responses were induced under actions of intrinsic pH buffers. A PKC inhibitor, staurosporine (1 $\mu$M), inhibited the effects of PMA on both current density and $\tau_{act}$ ($p < 0.01$; Figs. 3B and 3C). The deactivation time constant ($\tau_{tail}$), calculated from the single exponential fit for the tail current, was slowed by 1–1.6 $\mu$M PMA with a factor of 1.9 ± 0.3 ($n$ = 7; Figs. 2A and 3A). Under the physiological solutions, a factor of PMA (1 $\mu$M)-induced increase of the $H^+$ current amplitude (2.4 ± 0.4; $n = 7$) was smaller than that recorded with the solutions omitting $Na^+$, $K^+$, and $Cl^-$ ($p < 0.05$). The $\tau_{act}$ was decreased by a factor of 0.53 ± 0.10 ($n = 9$), but there was no significant difference between the two conditions.

PMA often induced inward currents at the holding potential (−60 mV; Figs. 3A and 3D). The inward current was reverted by diphenylene iodinium (DPI; 10 $\mu$M), an inhibitor for NADPH oxidases (Fig. 3E) and was therefore the most likely electron current ($I_e$) generated through activation of NADPH oxidases as reported in phagocytes.[13] However, the $I_e$ was not essential to activate the $H^+$ current, because DPI had no significant effects on the PMA-induced changes in the $H^+$ current density and $\tau_{act}$ (Figs. 3B and 3C).

### *ΔpH-dependent and -independent mechanisms responsible for PMA-induced potentiation of the $H^+$ current*

The *I-V* curve of the $H^+$ current was shifted toward more negative potentials by PMA (Fig. 4A). The plot of the average chord conductance ($g_H$) for the steady-state current shows that PMA shifted the voltage dependency for activation to a negative direction (Fig. 4B). The shift of half-activation voltage ($V_{1/2}$) estimated from the Boltzmann equation (lines) by 1–1.6 $\mu$M PMA was −35 ± 10 mV ($n$ = 11). In the permeabilized patch, voltage-gated inward currents were often recorded at potentials negative to $V_{rev}$ (Fig. 4A, inset), suggesting that $H^+$ could enter the cell. The $V_{rev}$ was shifted to more negative voltages by PMA.

The negative $V_{rev}$ shift implies increases in ΔpH, which enhances the $H^+$ current. However, even when $g_H$ was replotted against the driving force for $H^+$ ($V_m - V_{rev}$), the effects of PMA still remained (Fig. 4C): PMA increased the current density (Fig. 4D) and decreased $\tau_{act}$ (Fig. 4E) significantly. The potentiation ratio for the current density was 2.7 ± 0.5 ($n$ = 13) with 1–1.6 $\mu$M PMA. Although the amount varied among cells, this ΔpH-independent activation was observed in ~80% cells tested. These data suggest that both ΔpH-dependent and -independent mechanisms may participate in the PMA-induced activation of the $H^+$ channel.

### *PMA-induced cell acidosis in clamped and nonclamped cells*

When $pH_o$ is maintained to be constant, $pH_i$ could be estimated from $V_{rev}$ from the linear correlation between $V_{rev}$ and ΔpH (Fig. 1F). In the permeabilized patch, $V_{rev}$ at $pH_o$ 7.3 was 23 ± 4 mV ($n$ = 41), indicating that the $pH_i$ was

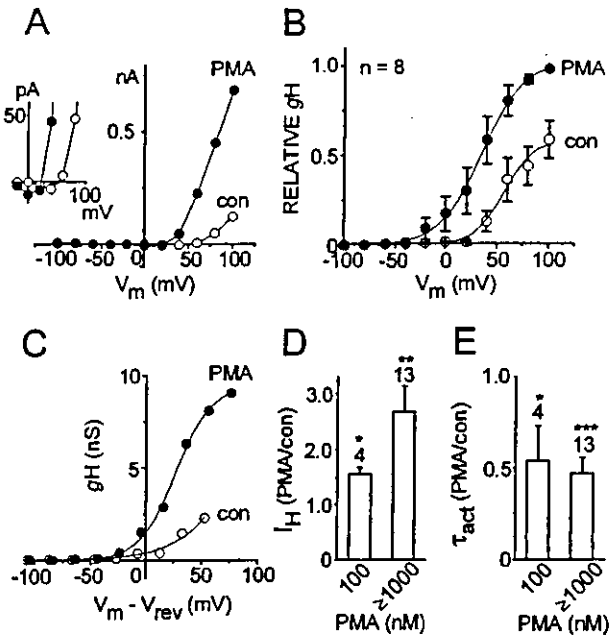


FIG. 4. PMA-induced shifts of the *I-V* relationship and $V_{rev}$. (A) The *I-V* curves for the $H^+$ currents measured at 4 s of voltage steps applied at −60 mV. PMA shifted $V_{rev}$ to more negative potential (inset). Small inward currents were recorded at voltages negative to $V_{rev}$. (B) Averaged chord conductance ($g_H$), calculated by dividing the steady-state currents by the driving force ($V_m - V_{rev}$), are plotted against $V_m$. When the $H^+$ current did not reach the steady state during depolarization, it was estimated from the single exponential fit for the data. Data were normalized by the maximum value in each cell. (C) PMA-induced changes in $g_H$ plotted against $V_m - V_{rev}$. A and C were obtained from the same cell. (D and E) PMA-induced increased ratio of the (E) current density and (F) decreased ratio of $\tau_{act}$ at $V_{rev}$ + 40 ~ 80 mV. The data were compared at the same driving force in each cell. $^*p < 0.05$, $^{**}p < 0.01$, and $^{***}p < 0.001$ compared with the values with no PMA (paired $t$-test). The bath contained NMDG aspartate and 100 $\mu$M DIDS. The pipette contained Cs-methanesulfonate. $pH_i/pH_o$ = 5.5–7.6/7.3.

estimated to be 7.69 ± 0.06 ($n$ = 41). This alkaline $pH_i$ coincided well with the resting $pH_i$ in intact cells measured by a pH fluorescent dye, BCECF (7.59 ± 0.03; mean ± SE, $n$ = 45), and with that reported in rabbit osteoclasts.[28]

The PMA-induced $V_{rev}$ shift to more negative potentials suggested that $pH_i$ was decreased by PMA. The PMA-induced cell acidosis was confirmed in intact cells with BCECF in the $Na^+$-containing standard Ringer solution (Fig. 5A). The decrease in $pH_i$ at 10 minutes of perfusion with 10, 100, and 1000 nM PMA was −0.07 ± 0.05 ($n$ = 12), −0.12 ± 0.03 ($n$ = 20), and −0.25 ± 0.02 U ($n$ = 20; Fig. 5B). Staurosporine (1 $\mu$M) inhibited the cell acidosis (Fig. 5B; $p < 0.01$), implying that PKC mediated the PMA-induced cell acidosis. In the presence of $Zn^{2+}$, 1 $\mu$M PMA decreased $pH_i$ by 0.37 ± 0.06 U ($n$ = 14), implying that the $H^+$ channel was activated by the cell acidosis but not vice versa. There was no significant effect of DPI (10 $\mu$M) on either cell acidosis (Fig. 5B) or the $V_{rev}$ shift (Fig. 5C).

With the pipette and bath solutions omitting other ions, the $V_{rev}$ shift by 1–1.6 $\mu$M PMA (−23 ± 7 mV, $n$ = 12; Fig. 5C) corresponded to a decrease in $pH_i$ by 0.49 ± 0.14

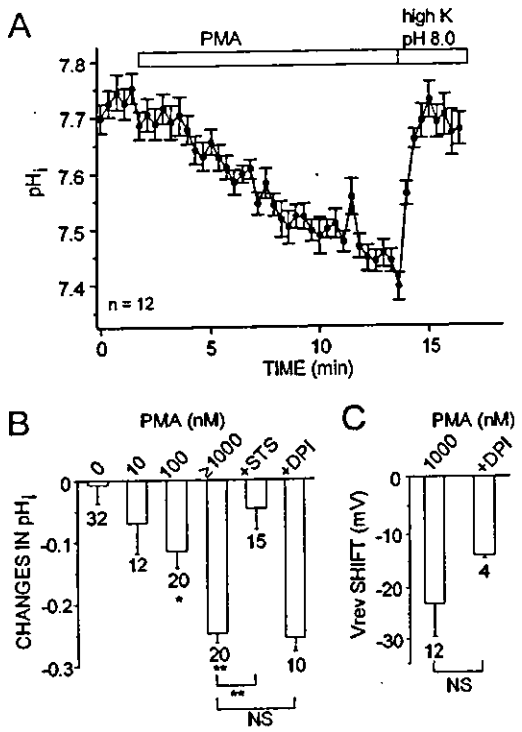


FIG. 5. PMA-induced cell acidosis. (A) PMA (1 $\mu$M)-induced changes in the intracellular pH ($pH_i$) measured with BCECF in single nonclamped cells bathed in the standard Ringer solution (means ± SE). The pH recovered quickly by replacing the medium by a $K^+$-rich, alkaline solution (pH 8.0). (B) Changes in $pH_i$ at 10-min perfusion of 10, 100, and 1000 nM PMA in the Ringer solution. Staurosporine (1 $\mu$M) or DPI (10 $\mu$M) were coapplied with 1 $\mu$M PMA. $*p < 0.05$, $**p < 0.01$ compared with the values with no PMA. (C) PMA (1–1.6 $\mu$M)-induced $V_{rev}$ shift in clamped cells in the presence and absence of DPI (10 $\mu$M). The bath contained NMDG aspartate and 100 $\mu$M DIDS. The pipette contained Cs-methanesulfonate. $pH_p/pH_o$ = 5.5–7.6/7.3.

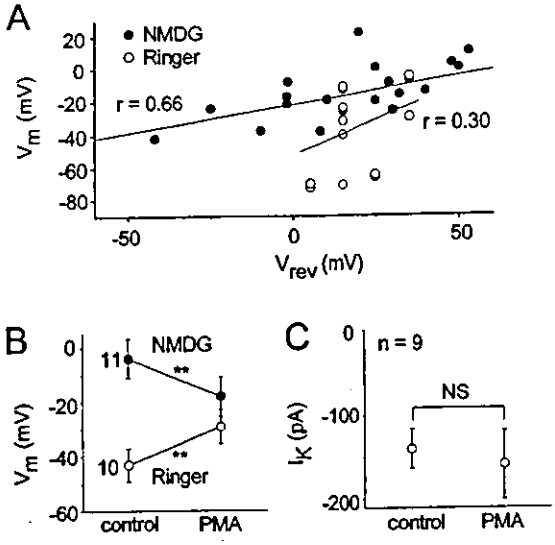


FIG. 6. Relationship between $V_{rev}$ and $V_m$. (A) Relationship between $V_{rev}$ and $V_m$ in the permeabilized patches before stimulation. Open ($n$ = 16) and closed symbols ($n$ = 20) represent data with and without the $K^+$ channel activity. The former was obtained from eight cells bathed in Ringer solution with the pipette containing K-gluconate, and the latter, from 20 cells in the NMDG aspartate solution with the pipette containing Cs-methanesulfonate. (B) The membrane potential before and after application of PMA (100–1000 nM) in the Ringer (open circles) and NMDG aspartate (closed circles) solutions. $**p < 0.01$ (paired $t$-test). (C) No significant effects of PMA (100–1000 nM) on the $K^+$ current amplitude at −100 mV.

U, almost double the value obtained with BCECF. The $V_{rev}$ shift was, however, −11.0 ± 2.4 mV ($n$ = 5) under physiological conditions. This decrease in $pH_i$ (−0.23 ± 0.05 U, $n$ = 5) was identical to the values measured with BCECF. Progression of the PMA-induced acidosis was reverted quickly in a $Na^+$-free $K^+$-rich alkaline medium that offered a favorable condition for activating the $H^+$ channel (Fig. 5A). Although actions of PMA may be irreversible, activation of the $H^+$ channel could rescue cells from continued acidosis.

### *Potentiation of the $H^+$ current activity moves the membrane potential toward $V_{rev}$*

A major resting conductance of murine osteoclasts is an inwardly rectifying $K^+$ ($IR_K$) current.[25] The membrane potential recorded in the permeabilized patch was −42 ± 7 mV ($n$ = 13) (min-max: −80 to −12 mV) under the physiological condition and −10 ± 3 mV ($n$ = 28) when the $IR_K$ current was eliminated. Without the $IR_K$ current, the resting $V_m$ had a positive correlation with $V_{rev}$ for the $H^+$ current (Fig. 6A, closed circles). With the $IR_K$ current, $V_m$ deviated to negative voltages (open circles), and contribution of the $H^+$ current to $V_m$ was smaller. In the presence of the $IR_K$ current, PMA (100–1000 nM) induced depolarization from −42 ± 6 to −29 ± 6 mV ($n$ = 10; Fig. 6B, open circles). However, PMA hyperpolarized cells from −4 ± 7 to −18 ± 7 mV ($n$ = 11) when the $IR_K$ current was eliminated (Fig. 6B, closed circles). Therefore, $V_m$ seemed to move toward $V_{rev}$ for the $H^+$ current. PMA (1 $\mu$M) had no significant effect on the $IR_K$ current (Fig. 6C) and increased $Cl^-$ currents only slightly, by a factor of 1.2 ± 1.0 ($n$ = 4).

## DISCUSSION

In this study, cell acidosis and activation of the $H^+$ channel were detected successfully using the permeabilized-patch recordings that allowed pH changes and preserved intracellular machinery in clamped cells. Phorbol ester (PMA) could generate a favorable condition for the channel activation by potentiating the $H^+$ channel activity and lowering the threshold, together with cell acidosis. The PMA-induced responses were mediated mainly through PKC, because they were inhibited by staurosporine.

### *PMA-induced activation of the $H^+$ channel of osteoclasts*

PMA increased the $H^+$ current amplitude and the activation rate, slowed decay of tail currents, and shifted the activation threshold to more negative potentials. These PMA-induced changes were similar in different ionic environments and in different cell-types,[14,17] indicating that the basic activating mechanisms are preserved. The channel

activation shifted the membrane potential toward $V_{rev}$. The direction of the shift depended on both the resting potential and $V_{rev}$. When the resting potential was lower than $V_{rev}$ because of the $K^+$ conductance, PMA depolarized cells, and when the resting potential was higher than $V_{rev}$, PMA hyperpolarized cells. In addition, PMA evoked DPI-sensitive inward currents, presumably electron currents ($I_e$) caused by electron transport through NADPH oxidases.[13] In phagocytes, the $H^+$ channels have been implicated to mediate $H^+$ efflux during respiratory bursts.[12,15,16] PMA is a strong activator for the oxidase.[14] Osteoclasts, originating from macrophage-lineage progenitors, also express NADPH oxidases.[29,30] The present data showed that PMA activated NADPH oxidases in osteoclasts but that the oxidases were not essential for the $H^+$ channel activation.

*PMA-induced cell acidosis*

Employing $V_{rev}$ as a real-time monitor for $pH_i$, PMA-induced cell acidosis was first confirmed in clamped cells. The PMA-induced cell acidosis was seen in the presence of DPI and much greater than the acidosis evoked by the NADPH oxidases in neutrophils,[31] suggesting that extrusion of electrons through the oxidase was not a major cause for the acidosis. Time required for half-maximal effects of PMA-induced potentiation of the $H^+$ current was often >5 minutes in osteoclasts, longer than that in eosinophils (2 minutes)[17] or neutrophils (3.4 minutes).[14] The gradual progress in cell acidosis might underlie the long-lasting channel activation in osteoclasts, because cell acidosis itself enhances the $H^+$ channel activity. Under physiological conditions, $Na^+$-dependent mechanisms, such as the $Na^+$-$H^+$ exchangers, may operate to increase $pH_i$. This may explain why the cell acidosis and the channel activation were milder than those obtained in the absence of extracellular $Na^+$. The $Na^+$-dependent mechanisms, however, could not cease the progression of the PMA-induced cell acidosis. It is noted that the cell acidosis was recovered immediately on activation of the $H^+$ channel.

*$\Delta pH$-independent mechanisms of the $H^+$ channel activation*

Is cell acidosis the only mechanism for the PMA-induced potentiation of the $H^+$ channel? We addressed the question by comparing data at the same driving force for $H^+$ and found that some of the increases in the current density and the activation rate remained in ~80% of cells tested. The pH-independent activation of the $H^+$ channel was reported in neutrophils[14] and eosinophils[17] but the underlying mechanisms remain unknown. Because the activity of NADPH oxidases is potent in these cells, the activating mechanisms might differ among cell types. In osteoclasts, cell acidosis and $\Delta pH$-independent pathways may activate the $H^+$ channel synergistically. An increase in the intracellular $Ca^{2+}$ concentration ($[Ca^{2+}]_i$) is reported to augment the $H^+$ current,[3] but PMA (1 $\mu$M) did not elevate $[Ca^{2+}]_i$ in osteoclasts (preliminary observation). Thus, the PMA-induced responses in osteoclasts were not mediated by a rise in $[Ca^{2+}]_i$. Cell acidosis generates cell swelling that is a potent activator for $H^+$ channels[5] and also a second message regulating osteoclast functions.[32,33] Modification of the cytoskeleton by PMA[19] may contribute to the channel activation.

*Physiological/pathological relevance*

Calcitonin[34,35] and extracellular $Ca^{2+}$ ($[Ca^{2+}]_o$)[36] are physiologic factors that modulate PKC in osteoclasts. Because these factors inhibit bone resorption, the activated $H^+$ channel would modulate the inhibition process. A rise in $[Ca^{2+}]_o$ induces cell acidosis,[37] cell swelling,[33,38] and depolarization by inhibiting the $K^+$ conductance.[25] All these factors are activators for the $H^+$ channel. The activated $H^+$ channel can revert depolarization and acidosis. Considering that cell acidosis evokes various responses in osteoclasts, such as swelling and sensitization of the $[Ca^{2+}]_o$-sensing mechanisms,[32,33,38] the $H^+$ channel might contribute to maintain the resorbing activity. Otherwise, the $H^+$ channel may play a role as a $H^+$-secreting apparatus in certain situations, such as inflammatory bone resorption: bone resorption is increased by interferon gamma, a stimulant of the NADPH oxidases,[30] which are potent activators for the $H^+$ channels in phagocytes. It is also noteworthy that the $H^+$ channel could operate as a $H^+$ influx pathway. When the resting potential is low from the $K^+$ conductance or when $V_{rev}$ is high from exposure to acids, $H^+$ influx may depolarize cells and transport $H^+$ from resorption pits. The membrane potential may be crucial in determining $[Ca^{2+}]_i$ during bone resorption[39] and volume regulation.[32,38]

The $H^+$ channel activity is probably more potent at physiological temperature.[10,11] The channel contributes to $H^+$ signaling in osteoclasts particularly at depolarization, but PMA lowered the activation threshold greatly. $K^+$ and $Cl^-$ channels are not essential to the PMA-induced activation of the $H^+$ channel but possibly modulate the process by regulating the membrane potential and cell volume. Other unidentified factors, either in physiological or pathological conditions, may enable the $H^+$ channel to be available over a wide range of the membrane potential of osteoclasts (−60–0 mV).[32]

## ACKNOWLEDGMENTS

We thank Drs Y Watanabe and F Nakamura for encouragement, Y Mogari for technical assistance, CH Kim for preparation of this manuscript, and T Akiyama for secretarial assistance. This work was supported by grants from The Assistant Program of Graduate Student Fellowships of Osaka City University, The Hoansha Foundation, and the Grant-in-Aid for Scientific Research from The Ministry of Education, Science and Culture, Japan.

## REFERENCES

1. Rousselle AV, Heymann D 2002 Osteoclastic acidification pathways during bone resorption. Bone **30**:533–540.
2. Kapus A, Romanek R, Qu AY, Rotstein OD, Grinstein S 1993 A pH-sensitive and voltage-dependent proton conductance in the plasma membrane of macrophages. J Gen Physiol **102**:729–760.
3. Holevinsky KO, Jow F, Nelson DJ 1994 Elevation in intracellular calcium activates both chloride and proton currents in human macrophages. J Membr Biol **140**:13–30.
4. Eder C, Fischer H-G, Hadding U, Heinemann U 1995 Properties of voltage-gated currents of microglia developed using macrophage colony-stimulating factor. Pflugers Arch **430**:526–533.

5. Morihata H, Nakamura F, Tsutada T, Kuno M 2000 Potentiation of a voltage-gated proton current in acidosis-induced swelling of rat microglia. J Neurosci **20**:7220–7227.
6. Nordström T, Rotstein OD, Romanek R, Asotra S, Heersche JN, Manolson MF, Brisseau GF, Grinstein S 1995 Regulation of cytoplasmic pH in osteoclasts. Contribution of proton pumps and a proton-selective conductance. J Biol Chem **270**:2203–2212.
7. Mori H, Sakai H, Morihata H, Yamano T, Kuno M 2002 A voltage-gated $H^+$ channel is a powerful mechanism for pH homeostasis in murine osteoclasts. Kobe J Med Sci **48**:87–96.
8. DeCoursey TE 2003 Voltage-gated proton channels and other proton transfer pathways. Physiol Rev **83**:475–579.
9. Andersen OS 2002 Perspective on the identity of the $H^+$ channel involved in the respiratory burst. J Gen Physiol **120**:757.
10. Kuno M, Kawawaki J, Nakamura F 1997 A highly temperature-sensitive proton current in mouse bone marrow-derived mast cells. J Gen Physiol **109**:731–740.
11. DeCoursey TE, Cherny VV 1998 Temperature dependence of voltage-gated $H^+$ currents in human neutrophils, rat alveolar epithelial cells, and mammalian phagocytes. J Gen Physiol **112**:503–522.
12. Henderson LM, Chappell JB, Jones OT 1987 The superoxide-generating NADPH oxidase of human neutrophils is electrogenic and associated with an $H^+$ channel. Biochem J **246**:325–329.
13. Schrenzel J, Serrander L, Bánfi B, Nüsse O, Fouyouzi R, Lew DP, Demaurex N, Krause KH 1998 Electron currents generated by the human phagocyte NADPH oxidase. Nature **392**:734–737.
14. DeCoursey TE, Cherny VV, Zhou W, Thomas LL 2000 Simultaneous activation of NADPH oxidase-related proton and electron currents in human neutrophils. Proc Natl Acad Sci USA **97**:6885–6889.
15. Nanda A, Grinstein S 1991 Protein kinase C activates an $H^+$ (equivalent) conductance in the plasma membrane of human neutrophils. Proc Natl Acad Sci USA **88**:10816–10820.
16. Kapus A, Szaszi K, Ligeti E 1992 Phorbol 12-myristate 13-acetate activates an electrogenic $H^+$-conducting pathway in the membrane of neutrophils. Biochem J **281**:697–701.
17. DeCoursey TE, Cherny VV, DeCoursey AG, Xu W, Thomas LL 2001 Interactions between NADPH oxidase-related proton and electron currents in human eosinophils. J Physiol **535**:767–781.
18. Lorenzo JA, Sousa S 1988 Phorbol esters stimulate bone resorption in fetal rat long-bone culture by mechanisms independent of prostaglandin synthesis. J Bone Miner Res **3**:63–67.
19. Teti A, Colucci S, Grano M, Argentino L, Zallone AZ 1992 Protein kinase C affects microfilaments, bone resorption, and $[Ca^{2+}]_o$-sensing in cultured osteoclasts. Am J Physiol **263**:C130–C139.
20. Williams JP, McKenna MA, Thames AM III, McDonald JM 2000 Tamoxifen inhibits phorbol ester stimulated osteoclastic bone resorption: An effect mediated by calmodulin. Biochem Cell Biol **78**:715–723.
21. Zhang ZY, Mühlbauer R, Felix R 1998 Phorbol myristate acetate downregulates the binding sites for colony-stimulating factor-1 on osteoclasts isolated form rats. Calcif Tissue Int **62**:148–152.
22. Mori H, Sakai H, Morihata H, Sakuta K, Kuno M 2001 A voltage-gated proton channel in murine osteoclasts during development from bone marrow cells. J Bone Miner Res **16**:S1;S377.
23. Niida S, Kaku M, Amano H, Yoshida H, Kataoka H, Nishikawa S, Tanne K, Maeda N, Nishikawa S, Kodama H 1999 Vascular endothelial growth factor can substitute for macrophage colony-stimulating factor in the support of osteoclastic bone resorption. J Exp Med **190**:293–298.
24. Suzuki K, Zhu B, Rittling SR, Denhardt DT, Goldberg HA, McCulloch CA, Sodek J 2002 Colocalization of intracellular osteopontin with CD44 is associated with migration, cell fusion, and resorption in osteoclasts. J Bone Miner Res **17**:1486–1497.
25. Shibata T, Sakai H, Nakamura F, Shioi A, Kuno M 1997 Differential effect of high extracellular $Ca^{2+}$ on $K^+$ and $Cl^-$ conductances in murine osteoclasts. J Membr Biol **158**:59–67.
26. Morihata H, Kawawaki J, Sakai H, Sawada M, Tsutada T, Kuno M 2000 Temporal fluctuation of voltage-gated proton currents in rat spinal microglia via pH-dependent and -independent mechanisms. Neurosci Res **38**:265–271.
27. Gordienko DV, Tare M, Parveen S, Fenech CJ, Robinson C, Bolton TB 1996 Voltage-activated proton current in eosinophils from human blood. J Physiol **496**:299–316.
28. Lees RL, Heersche JN 2000 Differences in regulation of $pH_i$ in large (≥10 nuclei) and small (≤5 nuclei) osteoclasts. Am J Physiol **279**:C751–C761.
29. Steinbeck MJ, Appel WH Jr, Verhoeven AJ, Karnovsky MJ 1994 NADPH-oxidase expression and in situ production of superoxide by osteoclasts actively resorbing bone. J Cell Biol **126**:765–772.
30. Darden AG, Ries WL, Wolf WC, Rodriguiz RM, Key LL Jr 1996 Osteoclastic superoxide production and bone resorption: Stimulation and inhibition by modulators of NADPH oxidase. J Bone Miner Res **11**:671–675.
31. Henderson LM, Chappell JB, Jones OT 1988 Internal pH changes associated with the activity of NADPH oxidase of human neutrophils. Further evidence for the presence of an $H^+$ conducting channel. Biochem J **251**:563–567.
32. Sakai H, Nakamura F, Kuno M 1999 Synergetic activation of outwardly rectifying $Cl^-$ currents by hypotonic stress and external $Ca^{2+}$ in murine osteoclasts. J Physiol **515**:157–168.
33. Sakuta K, Morihata H, Mori H, Sakai H, Kuno M 2002 Cell swelling as an intermediate signal leading to activation of a $Cl^-$ channel in extracellular calcium-sensing of murine osteoclasts. Osaka City Med J **48**:29–38.
34. Samura A, Wada S, Suda S, Iitaka M, Katayama S 2000 Calcitonin receptor regulation and responsiveness to calcitonin in human osteoclast-like cells prepared in vitro using receptor activator of nuclear factor-kappa B ligand and macrophage colony stimulating factor. Endocrinology **141**:3774–3782.
35. Su Y, Chakraborty M, Nathanson MH, Baron R 1992 Differential effects of the 3′, 5′-cyclic adenosine monophosphate and protein kinase C pathways on the response of isolated rat osteoclasts to calcitonin. Endocrinology **131**:1497–1502.
36. Kifor O, Diaz R, Butters R, Brown EM 1997 The $Ca^{2+}$-sensing receptor (CaR) activates phospholipase C, A2, D in bovine parathyroid and CaR-transfected, human embryonic kidney (HEK293) cells. J Bone Miner Res **12**:715–725.
37. Grano M, Faccio R, Colucci S, Paniccia R, Baldini N, Zallone AZ, Teti A 1994 Extracellular $Ca^{2+}$ sensing is modulated by pH in human osteoclast-like cells in vitro. Am J Physiol **267**:C961–C968.
38. Sakuta K, Sakai H, Mori H, Morihata H, Kuno M 2002 $Na^+$-dependence of extracellular $Ca^{2+}$-sensing mechanisms leading to activation of an outwardly-rectifying $Cl^-$ channel in murine osteoclasts. Bone **31**:374–380.
39. Shanker VS, Huang CLH, Adebanjo O, Simon B, Alam ASMT, Moonga BS, Pazianas M, Scott RH, Zaidi M 1995 Effect of membrane potential on surface receptor activation in rat osteoclasts. J Cell Physiol **162**:1–8.

Address reprint requests to:
*Miyuki Kuno, MD, PhD*
*Department of Physiology*
*Osaka City University Graduate School of Medicine*
*Abeno-ku*
*Osaka 545-8585, Japan*
*E-mail: kunomyk@med.osaka-cu.ac.jp*

Received in original form December 9, 2002; in revised form June 5, 2003; accepted July 16, 2003.

ELSEVIER

# Reversible Altered Consciousness With Brain Atrophy Caused by Valproic Acid

**Hideo Yamanouchi, MD*, Takako Ota, MD†, George Imataka, MD†, Eiji Nakagawa, MD*, and Mitsuoki Eguchi, MD***

**A 5-year-old female developed alteration of consciousness during 3 days of long-term treatment with valproic acid for localization-related epilepsy. Computed tomography revealed cerebral atrophy, and electroencephalography presented slow background activity. Consciousness cleared only 12 hours after valproic acid was discontinued, and normal electroencephalography results were evident 1 week later. Cerebral atrophy was nonexistent 2 months later. This rapidly developing but reversible alteration of consciousness in parallel with brain atrophy is recognized as a rare idiosyncratic adverse effect of valproic acid.** 

Yamanouchi H, Oka T, Imataka G, Nakagawa E, Eguchi M. Reversible altered consciousness with brain atrophy caused by valproic acid. Pediatr Neurol 2003;28:382-384.

## Introduction

Stupor or coma induced by valproic acid may be associated with hyperammonemia with or without hepatic dysfunction [1,2]. Different from this category, reversible cognitive and behavioral deterioration associated with a radiologic finding of brain atrophy has been reported as a rare adverse effect of valproic acid and is characterized by a subacute or chronic course without hyperammonemia [3-5]. Recovery occurs throughout weeks or months after discontinuation of valproic acid therapy. Reported here is valproic acid–related alteration of consciousness associated with brain atrophy that progressed throughout only 3 days and resolved within 12 hours after discontinuation of valproic acid.

## Case Report

This 5-year-old female was the product of a 39-week gestation and a normal delivery. She manifested normal developmental milestones. She remained healthy until aged 2 years, when she presented with drop episodes followed by unconsciousness for several minutes. Electroencephalogram (EEG) demonstrated normal background activity during the wakeful state and bilateral intermittent focal spikes throughout anterior temporal and central regions during sleep recording. She was diagnosed with localization-related epilepsy. Valproic acid was introduced at 10 mg/kg/day and maintained at 15 mg/kg/day. Blood-screening tests, including liver function tests, blood cell counts, and serum amylase assays, performed at 2 weeks and 2 months after valproic acid introduction, revealed normal findings. No seizures were observed at the above dose of valproic acid until the patient was 5 years of age, when a brief generalized clonic seizure occurred. Computed tomography (CT) disclosed normal findings (Fig 1A, B). Because the recurrent seizure was associated with a low serum concentration of valproic acid (25.7 μg/mL), the valproic acid dose was increased to 20 mg/kg/day, with a resulting steady-state serum concentration of 76.4 μg/mL.

After 3 months, she was admitted to the hospital because of alteration of consciousness, which developed throughout 3 days. Before this disturbance, mental and motor development had been normal, even after seizure onset. She could maintain arousal and was reactive to painful or tactile stimuli but had difficulty stating her name. She demonstrated little interest in her surroundings and hardly talked with her mother. She was not incontinent, agitated, or irritable. Physical and neurologic examination results were normal. Routine complete blood cell count was normal, as were levels of serum electrolytes, glucose, calcium, phosphate, urea nitrogen, creatinine, ammonia, lactate, and pyruvate; liver-function test results were normal, and carnitine, amino acid, and organic acid analysis yielded normal results. The serum valproic acid concentration was 107 μg/mL. CT indicated mild enlargement of cerebral sulci and pericerebral spaces; ventricular size was normal and no cerebellar or brainstem atrophy was observed (Fig 1C, D). EEG during wakefulness revealed diffuse slowing of background activity (Fig 2); a sleep recording depicted normal background activity.

Valproic acid treatment was discontinued on admission because of previous case reports linking it to reversible mental deterioration associated with brain atrophy [3-5]. The next morning, approximately 12 hours after admission, her consciousness level became completely normal. EEG repeated 1 week after valproic acid discontinuation manifested normal background activity during wakefulness, and no paroxysmal discharge was observed (Fig 3). Administration of phenobarbital was begun 10 days after the discontinuation of valproic acid. Serial CT

From the *Department of Pediatrics, Dokkyo University School of Medicine; and the †Department of Pediatrics, Shimotsuga General Hospital, Tochigi, Japan.

Communications should be addressed to:
Dr. Yamanouchi; Department of Pediatrics, Dokkyo University School of Medicine; 880 Kitakobayashi; Mibu, Shimotsuga;
Tochigi 321-0293, Japan.
Received July 25, 2002; accepted December 10, 2002.




doi:10.1016/S0887-8994(03)00005-5 • 0887-8994/03/$—see front matter

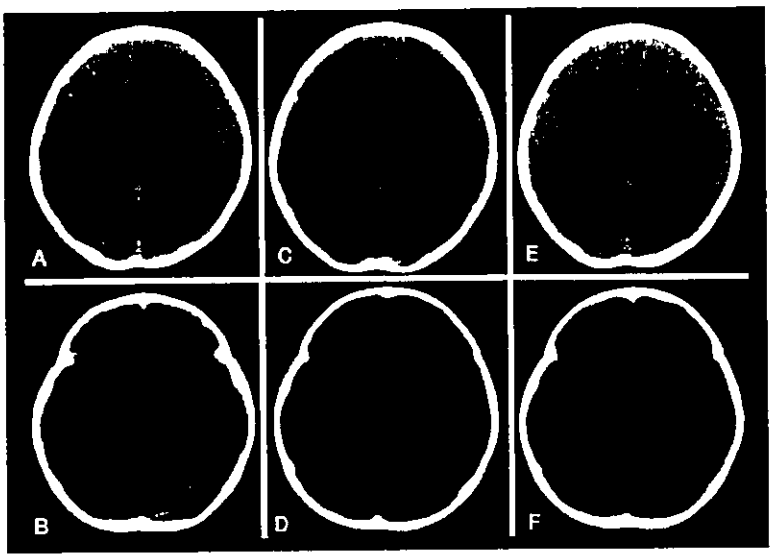


*Figure 1. Serial brain CT. (A, B) Two years before alteration in consciousness. (C, D) On admission. (E, F) Two months after discontinuation of valproic acid. Observe normal findings in A and B, as well as E and F, contrasting with mild atrophic changes in the cerebrum in C and D.*

demonstrated improvement in the atrophic change of the cerebrum 1 month later, followed by a complete return to normal after 2 months (Fig 1E, F). Subsequent magnetic resonance imaging revealed no significant change in the brain. On follow-up in the outpatient department 5 months after discontinuation of valproic acid, she manifested no abnormalities, and her parents described her behavior and mental function as entirely normal.

## Discussion

Rapidly developing alteration of consciousness associated with brain atrophy and its dramatic resolution after discontinuation of valproic acid treatment characterizes the clinical feature in this patient. EEG in the wakeful state revealed slowing background activity when the patient manifested altered consciousness, and EEG activity returned to normal when she recovered consciousness. Rapid depression of consciousness raises suspicion of valproic acid–related encephalopathy with hyperammonemia, which may occur in isolation [2] or in association with such underlying disorders as urea cycle enzyme deficiency [1]. Mitochondrial disorders such as MELAS (mitochondrial myopathy, encephalopathy, lactic acidosis, and strokelike episodes) [6] and cytochrome c deficiency with hepatic failure [7] can be triggered by valproic acid. Carnitine deficiency may predispose patients to encephalopathy upon initiation of valproic acid therapy [8]. Finally, paradoxic epileptogenic effects of valproic acid, particularly induction of nonepileptic-status epilepticus, also are part of the differential diagnosis [9].

This patient's clinical features and course were similar to those in previously reported pediatric cases [3-5] in which valproic acid was associated with reversible cognitive or behavioral deterioration and brain atrophy. Such states often persist for months, with reduction or disappearance of mental deterioration requiring weeks ([3]; patient 1 in [4]; [5]) or even months (patient 2 in [4]). Compared with those described in these reports, this patient appears to be unique in that clinical manifestations developed throughout only 3 days and disappeared only 12

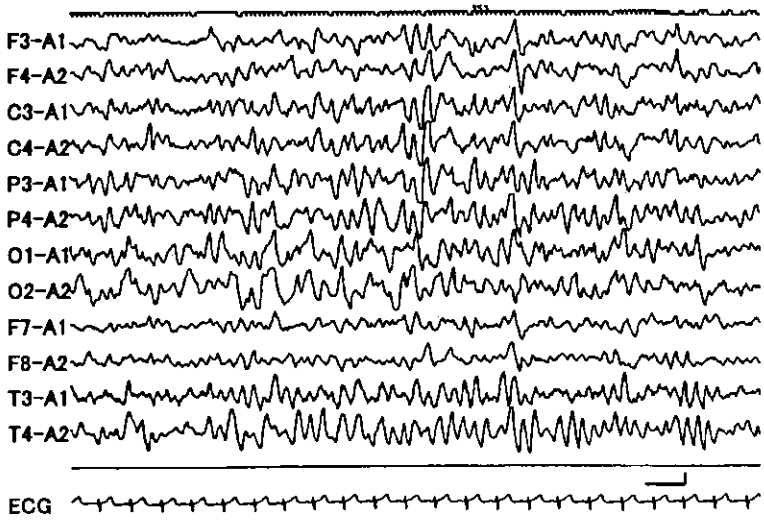


*Figure 2. Waking electroencephalography on admission, revealing diffuse slowing of background activity. Calibration marks: 1 second, 100 μV.*